Engineered Metalloproteins as Contrast Sensors for Molecular fMRI

By

Victor S. Lelyveld

A.B. Biochemical Sciences
Harvard University, 2003

SUBMITTED TO THE DEPARTMENT OF BIOLOGICAL ENGINEERING IN PARTIAL FULFILLMENT OF THE REQUIREMENTS FOR THE DEGREE OF

DOCTOR OF PHILOSOPHY IN BIOLOGICAL ENGINEERING
AT THE
MASSACHUSETTS INSTITUTE OF TECHNOLOGY

SEPTEMBER 2009
[February 2010]

Signature of Author: _____
Department of Biological Engineering
September 28, 2009

Certified by: _____
Alan P. Jasanoff
Associate Professor of Biological Enginering,
Nuclear Science and Engineering, and Brain and Cognitive Sciences
Thesis Supervisor

Certified by: _____
Peter C. Dedon
Professor of Toxicology and Biological Engineering
Chairman, Course XX Graduate Program Committee

Thesis Committee

Accepted by.....Douglas Lauffenburger
Whitaker Professor of Biological Engineering, Chemical Engineering, and Biology
Chairman of Thesis Committee

Accepted by.....Alan P. Jasanoff
Associate Professor of Biological Enginering,
Nuclear Science and Engineering, and Brain and Cognitive Sciences
Thesis Supervisor

Accepted by.....Kimberly Hamad-Schifferli
Assistant Professor of Biological Engineering
Thesis Committee Member

Engineered Metalloproteins as Contrast Sensors for Molecular fMRI

By

Victor S. Lelyveld

Submitted to the Department of Biological Engineering
On September 23, 2009 in Partial Fulfillment of the
Requirements for the Degree of
Doctor of Philosophy in Biological Engineering

ABSTRACT

Functional brain imaging technologies seek to expand our understanding of intact neural systems. Present day functional MRI (fMRI) measures the delayed hemodynamic response that is indirectly associated with neural activity. To study underlying molecular systems noninvasively but precisely, tools must be developed to modulate MRI contrast as a function of discrete molecular events within pathways of interest. In optical imaging modalities, genetically encoded sensors based on fluorescent proteins have provided an engineerable platform on which to optimize desirable device characteristics by exploiting the tools of molecular biology and protein biochemistry. Analogously, we seek to build genetically encodable sensors based on engineered metalloproteins whose effects on MRI contrast are regulated by specific biochemical interactions.

In this work, we present two technological advancements toward realizing fMRI contrast sensors for molecular neuroimaging. First, a genetically encodable sensor for free calcium is described, consisting of a novel ferritin-based device that reversibly enhances NMR transverse relaxation times (T_2) by Ca^{2+}-dependent crosslinking. Second, we show that the T_1 contrast effect of a recently proposed family of cytochrome P450-based MRI sensors can be significantly enhanced by substitution of the protein's native heme with a high spin manganese porphyrin.

Thesis Supervisor: Alan P. Jasanoff
Title: Associate Professor of Biological Engineering, Brain and Cognitive Sciences and Nuclear Science and Engineering

Incomplete Acknowledgements

Future generations of scientists will try and fail to calculate the enormity of my indebtedness to others for their support and guidance in pursuing this work. Preliminarily, I can say with reasonable certainty that I would not be here today were it not for my loving and supportive parents. Their idealism and ability are the standards by which I measure the world.

I owe a great debt to Alan Jasanoff, my advisor in this work, from whom a large majority of the ideas and successes of these efforts derive. I came to Alan not much more than a year prior to this writing, and he generously offered support and a trajectory for my graduate career. Scientifically, Alan demonstrates an impressive working knowledge that spans a diverse range of fields, applying an active mind toward overcoming daily hurdles. He has an honest, confident, and unimposing style of advising that acknowledges our shared goals in the process of science. My fellow Jasanoff lab-mates and alumni are also deserving of thanks—most especially Mikhail Shapiro, without whom none of the work presented here would have been possible.

For germinating and sustaining the environment in which I have been privileged to carry out my graduate studies, Doug Lauffenburger deserves my deepest gratitude. He has consistently shown me a personal supportiveness and positivity that serves as a model for the leadership of a community. To Kim Hamad-Schifferli and former lab-mates Josh Alper, Kate Brown, and Shahriar Khushrushahi among others, I wish them the best of luck in all their endeavors and give thanks for nucleating my exposure to the engineering of very small stuff.

My classmates in BE 2003 and too many supportive friends and housemates have forged great memories of my time here. Andrew Khouri, Barry Canton, and Jason Kelly have doggedly perpetuated my childhood far longer than should be legally permissible. Your mothers would all be proud.

For Shan, I do not yet have satisfactory words to convey my gratitude, but I am committed to spending my life in their pursuit.

Table of Contents

1 Introduction 11

1.1 Overview 11

1.2 Toward a systems-level understanding of neuroscience 12

1.3 fMRI and BOLD fMRI 13

1.4 Engineering contrast sensors for molecular fMRI imaging 15

1.4.1 Proton NMR relaxation processes 15

1.4.2 Models of T_1 and T_2 relaxivity enhancement by MRI contrast agents 17

1.4.3 Biochemical modulation of relaxivity enhancement 21

1.4.4 A protein engineering approach 23

2 Design and demonstration of a genetically encodable T_2 MRI sensor for Ca^{2+} dynamics 26

2.1 Overview 26

2.2 Introduction 26

2.3 Design 32

2.4 Results 33

2.4.1 A calmodulin-ferritin fusion protein can be synthesized in E. coli when coexpressed with untagged heavy chains 33

2.4.2 A tetrameric DsRed-RS20 fusion protein can be synthesized in E. coli and self-associates 38

2.4.3 Recombinant sensor components reversibly aggregate and accelerate T2 relaxation as a function of calcium concentration, stoichiometry, and crosslinker pI 40

2.4.4 DsRed-RS20-1.1 crosslinker-mediated CaM-ferritin aggregation is robust to the presence of detergent-free cell lysate in vitro. 44

2.4.5 CaM-FtH/FtH expression accelerates T_2 relaxation rates of transiently transfected human lung adenocarcinoma cells 45

2.4.6 Cells transiently transfected with the sensor show a change in subcellular fluorescence localization on treatment with a calcium ionophore 47
2.5 Discussion and Conclusions....49
2.6 Materials and Methods....51
2.6.1 Cloning of DsRed-RS20 and CaM-ferritin fusion proteins....51
2.6.2 Recombinant protein expression and purification....53
2.6.3 Dynamic light scattering (DLS)....55
2.6.4 MRI relaxometry....55
2.6.5 Mammalian tissue culture, transfection, and ionomycin treatment....56
3 Toward practical small molecule T_1 sensors: Improving the longitudinal relaxivity of *Bacillus megaterium* Cytochrome P450 BM3h....57
3.1 Introduction....57
3.2 Design....62
3.3 Results....64
3.3.1 BM3h apoprotein can be only partially reconstituted with MnPPIX in vitro....64
3.3.2 BM3h bacterially expressed in iron-free media can be refolded in lysate by addition of MnPPIX....66
3.3.3 Coexpression of O157:H7 ChuA with BM3h variants in MnPPIX-supplemented minimal media results in refolded MnBM3h proteins with improved T1 relaxivity....67
3.3.4 MnBM3h-B7 retains a low dopamine binding affinity and an associated relaxivity effect....71
3.4 Discussion and Future Directions....73
3.5 Materials and Methods....75
3.5.1 Expression and purification of recombinant BM3h proteins....75
3.5.2 In vitro production of BM3h apoprotein, and affinity chromatographic reconstitution with MnPPIX....76
3.5.3 Concentration determination for BM3h and MnBM3h proteins....77

3.5.4 Circular dichroism spectrometry 77

3.5.5 Recombinant production of Mn(III)-substituted BM3h protein by apoprotein refolding in bacterial lysates 78

3.5.6 Cloning and expression of the bacterial heme transporter ChuA 78

3.5.7 Recombinant production of Mn(III)-substituted BM3h protein by ChuA heme transporter coexpression 79

3.5.8 MRI relaxometry 80

3.5.9 Spectrophotometric and relaxometric ligand titration with MnBM3h proteins 80

4 Conclusions 82

5 References 86

1 Introduction

1.1 Overview

Functional imaging is a critical tool for unraveling the complex systems of the brain. Work to associate stimuli with brain activity has flourished particularly with the discovery of a blood oxygen level dependent (BOLD) effect on MRI signal only two decades ago [1]. Despite these rich returns, notable concerns remain as to the linearity, uniformity, and interrogative scope of the linkage between neural activation and changes in blood flow [2]. Since the BOLD response only reflexively indicates vascular compensation for brain activity [3], it is apparent that the precise molecular and cellular events in neural processing—and thus the critical questions in neuroscience—cannot be interrogated via the BOLD response alone. Alternatively, the ideal manifestation of a neuroactivity measurement device would be one that noninvasively senses electrochemical dynamics with high spatial and temporal resolution [4]. Toward analogous goals, molecular biology and protein biochemistry have produced instructive successes in molecular sensing, especially for application in optical imaging modalities [5,6], demonstrating that protein is a uniquely suited substrate on which to design molecular-level devices in biological contexts. In this thesis, we present two technological advances that approach the goal of creating engineered protein devices that can be detected noninvasively and that sense molecules functioning directly in the neurobiology of brain activity.

1.2 Toward a systems-level understanding of neuroscience

In its recent history, neuroscience has sought to integrate fascinating lessons derived from behavioral neuroscience with the mechanistic detail unearthed by neurobiologists at the molecular and cellular levels. Now, with the application and advancement of new technologies [7,8,9], the field is nearing a critical convergence of its various subdisciplines. The crossroads is likely to be found in the advancement of engineering approaches that seek to computationally integrate the vast connectivity and regulatory information of complex biological systems. Rather than serially studying relationships between behaviors and a small set of molecules, cells or brain structures, new technologies enable researchers to probe the complex pattern of connectivities and molecular processes underlying neural function. Concurrent with the rise of informatics analyses in systems biology, neuroscience will benefit from approaches that probe holistic networks of molecular and cellular processes, ultimately generating systematic models with predictive power [10].

Efforts in this direction are already underway. Genetic methods to probe and analyze neural circuitry have yielded fascinating insights into the complex organization of neuronal circuitry [11], including a complete mapping of synaptic contacts arising from single neurons [12]. To take full advantage of such tools requires correlating electrophysiological data of direct neuronal activation with advanced imaging modalities capable of answering spatiotemporal questions noninvasively *in vivo* [13,14]. So far, these technologies include positron emission tomography (PET) [7], optical tomography [15], and functional magnetic resonance imaging (fMRI). The last of these techniques has a unique advantage for neuroimaging because adequate spatial (<100 μm) and temporal (<1 s) resolution is routinely achievable over the field of view of the whole brain [2]. However, the interrogative scope of

current fMRI methods is, as we shall see, limited by the nature of the contrast mechanism currently in widespread use [8].

1.3 fMRI and BOLD fMRI

Envisioned as an analytical technique, fMRI is a method for observing functional processes by measuring the nuclear magnetic resonance (NMR) signal resolved in space and time. As it is primarily conceived of today, fMRI relies upon the endogenous oxygen sensor hemoglobin. Linus Pauling was the first to observe that oxygen-bound hemoglobin is diamagnetic, whereas unbound deoxyhemoglobin is paramagnetic [16]. Since hemoglobin concentration is at millimolar concentrations (around 150 g/L) in whole blood [17], small changes in the concentration of oxyhemoglobin within a blood-supplied tissue result in measurable changes in NMR signal intensity in T_2-weighted imaging sequences [1].

This observation is the basis of the blood oxygen level dependent (BOLD) response (Figure 1). It has been proposed that a tight coupling exists between energy-dependent processes in neurons, cellular respiration, and blood supply [3]. The model suggests that neural activity and associated respiration results in an increased local demand for oxygen from nearby vasculature. Initially, a short local transient in deoxyhemoglobin is followed by subsequent vasodilation that compensates for oxygen demand with augmented blood flow and volume, locally increasing the diamagnetic oxyhemoglobin content of nearby tissue. This results in a measurable decrease in local T_2 relaxation rates and therefore an increase in NMR signal intensity in T_2-weighted images (Figure 1a). These compensatory vascular effects are collectively termed "hemodynamic" responses [8,18].

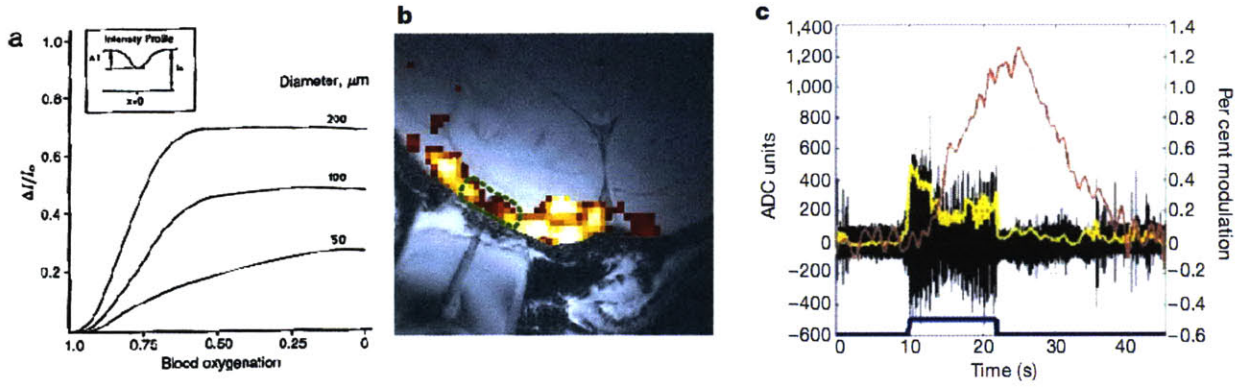

Figure 1. BOLD fMRI measures the delayed hemodynamic response after neural activity. (a) Changes in blood oxygenation fraction and vascular diameter modulate T2-weight signal intensity, as initially observed by Ogawa et al. (Adapted from [1]). (b, c) Logothetis et al. present a validation of the relationship between microelectrode-recorded local field potentials and the delayed BOLD response in monkey visual cortex during rotating checkerboard-pattern stimulation. In (c), raw (black) and root-mean-square (yellow) electrical signals are plotted alongside BOLD response (red) in the indicated region of interest in (b). Adapted from [19].

However, questions remain about the detailed mechanistic linkage between hemodynamics and neural activity in functional contexts [2,4]. While the relationship between the BOLD signal and electrical measurements evoked by short stimuli has been directly observed in the monkey visual cortex to be, in essence, a linear filtering of local field potentials [19] (Figure 1b,c), the linearity and spatiotemporal homogeneity of the relationship has been less apparent elsewhere [20,21,22]. Interpretation of fMRI "activation maps" is complicated by the coarse connection between hemodynamics and underlying processes occurring within microcircuits of any apparently activated voxel. Specifically, both excitatory and inhibitory effects can result in increased metabolic demand, as well as concurrent increases excitation and inhibition [8]. Conservatively, even when independently validated within a specific experimental context, BOLD fMRI can at best phenomenologically indicate regional processes acting in a manner correlating with a behavior or stimulus within the region and conditions specifically validated [21]. Accordingly, it may never be able to deconstruct satisfactorily—

without the aid of other more invasive and disruptive techniques—the underlying mechanism of neurological processes that span into unvalidated spatial regions and experimental conditions.

The Achilles' heel of present day the fMRI technique, therefore, lies not in the technological capabilities of the imaging modality, but rather in the limited interrogative power of the physiological contrast mechanism underlying the BOLD effect. We believe that newly engineered contrast agents for *molecular* fMRI can overcome this limitation. Specifically, our group has recently advanced the notion that direct molecular measurements can be taken with the aid of molecular sensors whose contrast enhancement is modulated as a function of specific chemical events [14].

1.4 Engineering contrast sensors for molecular fMRI imaging

1.4.1 Proton NMR relaxation processes

Classical "static" MRI contrast agents are paramagnetic substances that modulate the relaxation times of excited nuclear spins. Since there are two dominant relaxation processes, dubbed longitudinal (T_1) and transverse (T_2) relative to the direction of an applied static magnetic field, methods have been developed to both weight images and enhance contrast in manners dominantly associated with one relaxation process or the other [23].

When a population of proton spins is placed in a static magnetic field, $\boldsymbol{B_0}$, the net magnetic moment of the population slowly aligns with the direction of the field at a rate $R_1 = 1/T_1$. While the net

moment aligns directly along the field lines of $\boldsymbol{B_0}$, individual spin moments are precessing[1] about the field lines at a characteristic frequency that is called the Larmour frequency, ω_l. Since there is a Zeeman energy[2] difference between spins dominantly precessing aligned with $\boldsymbol{B_0}$ and those aligned against $\boldsymbol{B_0}$, a Boltzmann distributed subset of spins is precessing dominantly in the lower energy configuration, parallel to the field.[3] An RF pulse applied at precisely this resonance frequency can flip the population of spins into the higher energy configuration, turning the net magnetization vector of the population some angle away from $\boldsymbol{B_0}$, depending on the power and length of the applied pulse. Initially, this net moment coherently precesses around $\boldsymbol{B_0}$ with a component of its magnetization in an orthogonal or "transverse" plane. A coherent signal from this effect can be detected as a sinusoid by a nearby receiver coil. As the system then equilibrates to a low energy state, two relaxation processes take place. First, local spin-spin interactions and field inhomogeneities cause a loss of coherence in the transverse component of the magnetization, a process known as "dephasing" that occurs at a rate $R_2 = 1/T_2$. Second, the net moment of the magnetization slowly realigns with $\boldsymbol{B_0}$ by exchanging energy with the surrounding "lattice" and recovers its longitudinal magnetization vector in the direction of $\boldsymbol{B_0}$ at a rate R_1.

Since T_1 relaxation results in magnetization recovery in the longitudinal direction, brighter voxels in T_1-weighted images are those with faster T_1 relaxation times, such that more signal can be flipped into the transverse plane every at every repetition time-step, TR. Since T_2 relaxation is a decaying process, shorter T_2 relaxation times cause a loss in signal for at an observed echo time, TE, and therefore voxels with faster T_2 relaxation rates appear darker than those with slower rates.

---

[1] The classical macroscopic analogy for precession of the azimuthal spin angular momentum vector is the observation that a spinning top or gyroscope spins on its azimuthal axis while its axis, in turn, rotates about the axis of Earth's gravitational field lines.

[2] Zeeman energy refers to an energy difference between eigenstates of the quantized spin angular momentum that is amplified linearly by an applied magnetic field of increasing strength. At zero applied field, these states are degenerate.

[3] In fact, this is a loosely defined explanation from a quantum mechanical perspective, since all spins are strictly in a linear combination of both the parallel and antiparallel eigenstates. In general, we choose to invoke a classical explanation of the observable physics that is essentially a microscopic analogy inferred from the behavior of a macroscopic population of spins.

Contrast agents generally accelerate NMR relaxation rates. Accordingly, T_1 contrast agents brighten signal on T_1-weighted images, whereas T_2 contrast agents darken signal on T_2-weighted images. The extent of this effect is observed by measuring relaxation rate, R_1 or R_2, in some medium as a function of contrast agent concentration. This slope of these relationships is a molar relaxation rate constant, or relaxivity, r_1 or r_2. As theory has developed to describe the effects of contrast agents on NMR relaxation, so too have molecular sensors whose relaxivity is modulated by specific chemical events [4]. To understand mechanisms by which we may engineer contrast sensors that have specific chemical sensitivity, it is instructive to explore, at least superficially, the theory that has been developed to describe contrast agent effects on NMR relaxation.

1.4.2 Models of T_1 and T_2 relaxivity enhancement by MRI contrast agents

In NMR, unpaired nuclear spins (e.g. protons) are excited by a pulse of energy matching their precession frequency in an applied magnetic field. The relaxation of excited nuclear spins to equilibrium, like all relaxation processes, relies on energy transfer to the surroundings. These relaxation processes are enhanced by interactions between the excited nuclear spin angular momentum and that of unpaired electron spins. The foundations for modern NMR relaxation theory in such paramagnetic systems are the electron spin-nuclear spin relaxation equations presented by Solomon, Bloembergen and Morgan (SBM) [24,25,26]. There is a rich history to advancements in paramagnetic relaxation enhancement theory which is well beyond the scope of this introduction, but an instructive 1987 review by Lauffer is an excellent resource for theory that pertains to paramagnetic ions with generally small moments [27]. Recent efforts led by Gossuin, Roch, Muller, and Gillis [28,29] based on Freed [30,31]

have extended SBM theory to the rapid proton relaxation processes in fluids containing larger-moment superparamagnetic and ferromagnetic species.

The dominant proton relaxation effects of magnetic species in solution are modeled by partitioning the problem into so-called "reaction spheres." The molar relaxation time constants, r_1 longitudinally or r_2 transversely, are the superposition of relaxivity subprocesses associated with each relevant reaction sphere. For many weakly paramagnetic radicals and ions, inner sphere effects on directly coordinated waters dominate relaxivity for paramagnetic centers with small moments. In the inner sphere, proton spins that can coordinate transiently with the paramagnetic center are rapidly relieved of the energy in their excited spin state by the sum of scalar coupling (indirect nuclear interaction via intervening electron spins) and stochastic dipole-dipole interactions mediated by electron spins. The relaxation rate of the recipient electron spins, the rotational reorientation of the paramagnetic complex, and the exchange rate of spins at coordination sites into the bulk then become the dominant factors facilitating nuclear relaxation for spin populations. In their most basic form, these inner sphere interactions are encompassed in the Solomon, Bloembergen, and Morgan (SBM) equations describing the longitudinal relaxation time constant, $1/T_{1M}$ for a water proton bound to a paramagnet with spin S = ½,

$$\frac{1}{T_{1M}} = S(S+1)\left\{\frac{2}{15}\frac{\gamma_I^2 g^2 \beta^2}{r^6}\left[\frac{7\tau_c}{1+\omega_S^2\tau_c^2}+\frac{3\tau_c}{1+\omega_I^2\tau_c^2}\right]+\frac{2}{3}\left(\frac{A}{\hbar}\right)^2\left[\frac{\tau_e}{1+\omega_S^2\tau_c^2}\right]\right\} \qquad (1),$$

which agrees reasonably well with experiment for low-spin paramagnetic species [27]. In this expression, S is the spin quantum number, $\hbar$ is the reduced Planck's constant, and g is the electronic g-factor, a dimensionless constant that relates the spin and magnetic moment of the electron. ω_I and ω_S are the NMR precession frequencies associated with the nuclear spin, I, and the electron spin, S, respectively. A is a constant describing the strength of scalar spin-spin coupling. The gyromagnetic

ratios γ_I and γ_S linearly relate $\omega_{I,S}$ to the static field strength B_0 and therefore govern the frequency necessary to excite spins for any given instrument. The distance, *r*, is the separation between the paramagnet and coordinated nuclear dipoles (i.e. the protons of bound water). As illustrated in slightly more detail by Lauffer and Kowalewski et al., the correlation times τ_c and τ_e account for several complex relaxation processes depending on the static field strength, the timescale of collisional distortions of the coordination complex, the zero-field electron spin relaxation times, T_{1e}, the chemical exchange lifetime of spins in the inner sphere coordination sites, τ_M, and the rotational correlation time, τ_R. (For paramagnetic species with $S >> ½$, the scalar coupling and dipole-dipole components have been modified to account for larger-moment effects. These updated modifications are explained in detail by Kowalewski and colleagues [32].) For small paramagnetic ions, then, the inner sphere longitudinal relaxivity is

$$r_{1,IS} = \frac{1}{T_{1,IS}} = q\left[\frac{P_M}{T_{1M} + \tau_M}\right] \qquad (2),$$

where P_M is the mole fraction of paramagnetic species in solution and q is the number of water coordination sites at the paramagnetic species.

It should be noted that, beyond protons in the innermost coordination sphere, spin coupling with uncoordinated "outer sphere" waters can superimpose significantly on the overall T1 relaxation rate. For reference, Lauffer outlines a general outer sphere model that is applicable to certain high symmetry scenarios, as follows:

$$r_{1,OS} = \frac{1}{T_{1,OS}} = S(S+1)\left[\frac{C\pi N_S \gamma_I^2 \gamma_S^2 \hbar^2}{d^3 \tau_D}\right][7I(\omega_S, \tau_D, T_{1e}) + 3I(\omega_I, \tau_D, T_{1e})] \qquad (3).$$

In this expression, the two frequency dependent terms are spectral density functions describing nuclear and electron scalar and dipolar coupling. As it relates to work described herein, the outer

sphere contributions also depend directly on *S(S+1)*. Therefore, the total spin of paramagnetic ions has a direct effect on T_1 relaxivity in both directly coordinated and nearby diffusing waters. Outer sphere T_1 relaxivity also depends inversely on the distance of closest approach of water protons to the paramagnet, *d*, and on the self-diffusion time constant, $\tau_D = d^2/3(D_I + D_S)$, of nearby waters, based on the diffusivity of water D_I, and that of the contrast agent, D_S.

Small paramagnetic ions are not often employed for transverse (T_2) relaxation enhancement in biological context, since the background T_2 relaxation times are already quite rapid (<100 ms) in tissue, whereas T_1 times in tissue are significantly longer (~1 second). T_2 contrast agents are more typically superparamagnetic iron oxide nanoparticles that have substantially larger magnetic moments and, thus, larger r_2. For these more magnetized species, effects on uncoordinated nuclear spins in the so-called "outer sphere" become important in T_2 relaxivity enhancement, and it is generally accepted for small particles that this process is dominated by the acceleration of transverse dephasing as protons diffuse through the heterogeneous local magnetic fields of the contrast agent [33]. However, generally validated theory to describe T_2 relaxation enhancement of small superparamagnetic nanoparticles as a function of applied field and temperature is still an active field of inquiry, although great strides have been made in recent years by the Belgian researchers Roch, Muller, Gillis, and Gossuin among others [28,29,34]. For outer sphere effects, it is reasonably well understood that T_2 relaxivity of superparamagnetic nanoparticles depends strongly on their magnetic moment, μ, on the diffusion timescale of water molecules, τ_D, within the resulting local magnetic field gradients, and on the echo time used for imaging.

Basing our methods on these theoretical underpinnings, our ambition is to develop MRI contrast sensors with variable contrast using protein as our material substrate. Therefore, we are primarily interested in understanding and engineering metalloproteins that confer contrast enhancement,

especially in a manner that could be varied by biochemical events. To do so, we turn our attention to the mechanisms by which we might modulate physicochemical parameters that govern the contrast enhancement of natural or engineered metalloproteins in a manner that is sensitive to specific biomolecules of interest.

1.4.3 Biochemical modulation of relaxivity enhancement

Among the various parameters in the inner sphere component of SBM theory, only a few can be dynamically modulated by chemical interactions in the context of biological systems. Since relaxation effects are a linear function of contrast agent concentration, several groups have sought to take advantage of the parameter P_M, the mole fraction of contrast media, using genetic means—that is, by exploiting a biological process to modulate the concentration of a contrast agent [35]. For instance, Koretsky and colleagues have demonstrated that the paramagnetic ion Mn^{2+} can act as a Ca^{2+} analog and accumulate in active brain structures *in vivo* [36,37]. However, perturbations brought about by exploiting mass transport, pharmacokinetics, or gene expression in a manner resulting in large concentration changes—on the order of 10^{-6} - 10^{-4} M—are generally quite slow in biological context—on the order of minutes to hours, if not longer—limiting the utility of such processes for observing rapid temporal dynamics [35,38].

Alternatively, other approaches to regulate relaxivity of contrast agents directly have been proposed. Since inner sphere longitudinal relaxation is governed by the coordination of water directly to the paramagnetic ion, the number of water coordination sites, q, is an overriding parameter for inner sphere relaxation. To exploit this mechanism, synthetic small molecule T_1 sensors for Ca^{2+} and Zn^{2+} have

been synthesized, in which selective chelation of the target inorganic ion regulates q on a coordinated paramagnetic ion, Gd(III) or Mn(III) [39,40,41]. However, it has not yet been demonstrated that this class of synthetic compounds is deliverable *in vivo* at the concentrations necessary for functional sensing of normal activity (approximately 10 - 100 μM) [14].

Species conferring strong T_2 relaxation enhancement are typically superparamagnetic nanoparticles containing thousands of iron atoms [42]. Efforts to regulate this contrast enhancement have focused on the effects of clustering or aggregation [34,43]. It has been observed that the transverse relaxation rate, R_2, of clusters exhibits a biphasic relationship dependent on the self-diffusion timescale of nearby water, τ_D, and on the echo time used for imaging [44]. For smaller aggregates, this effect is essentially a second-order function of the aggregate radius [34].

This effect has been exploited to produce a variety of T_2 contrast sensors based on synthetic superparamagnetic nanoparticles. For example, Perez et al. demonstrated that aggregation of superparamagnetic nanoparticles could be mediated by specific interactions with DNA and protein [43]. Furthermore, Atanasijevic et al. demonstrated that nanoparticles can be inducibly aggregated by Ca^{2+}, in a manner that can be tuned using the biochemical parameters of the immobilized protein species calmodulin (CaM) and its calcium-dependent binding partners [45]. However, since stoichiometry of the sensor components is critical to the aggregation response of this class of sensors, application *in vivo* would require tight control over the pharmacokinetics of each component to maintain them at an appropriate ratio for sensing. The synthetic complexity of nanoscale devices is typically cumbersome, and production of large quantities of functionalized nanoparticles for application *in vivo* is costly and time-consuming.

1.4.4 A protein engineering approach

Genetically encodable biochemical reporters and sensors have seen substantial success in fluorescence imaging modalities, an approach pioneered by Tsien, Miyawaki, and colleagues [6]. Genetic encodability presents the opportunity to target precise cell types, structures, and processes by taking advantage of viral and transgenic technologies [11,46]. Furthermore, enzymology and structural biology have produced a detailed understanding of the metalloproteins involved in diverse biological processes. Such mechanistic and structural knowledge can be employed in the process of rational device design [47], and evolutionary protein engineering approaches can then be exploited to refine desirable characteristics of the device using the tools of molecular biology [48,49].

To generalize, fluorescent protein sensors operate by perturbing fluorescence signal with specific allosteric binding events and conformational changes. An analogous approach to modulate proton relaxation contrast mechanisms could enable new technological possibilities for the magnetic resonance imaging modality. Along these lines, Shaprio et al. have demonstrated that the hemoprotein cytochrome P450 BM-3 has ligand-dependent q—and therefore T_1 relaxivity—and can be engineered to bind small molecules of interest to neurobiology [50], which we will discuss in greater detail as it pertains to Chapter 3. In this recent work, the authors selected dopamine-binding mutants by directed evolution, and rational site directed mutagenesis was then employed to improve thermostability. When bound to target ligand, engineered protein variants appeared to have $q = 0$, whereas unbound proteins had $q = 1$ (Figure 2a). The associated T_1 relaxivity change has been used to observe potassium-stimulated dopamine release in cultured cells and *in vivo* (see Chapter 3).

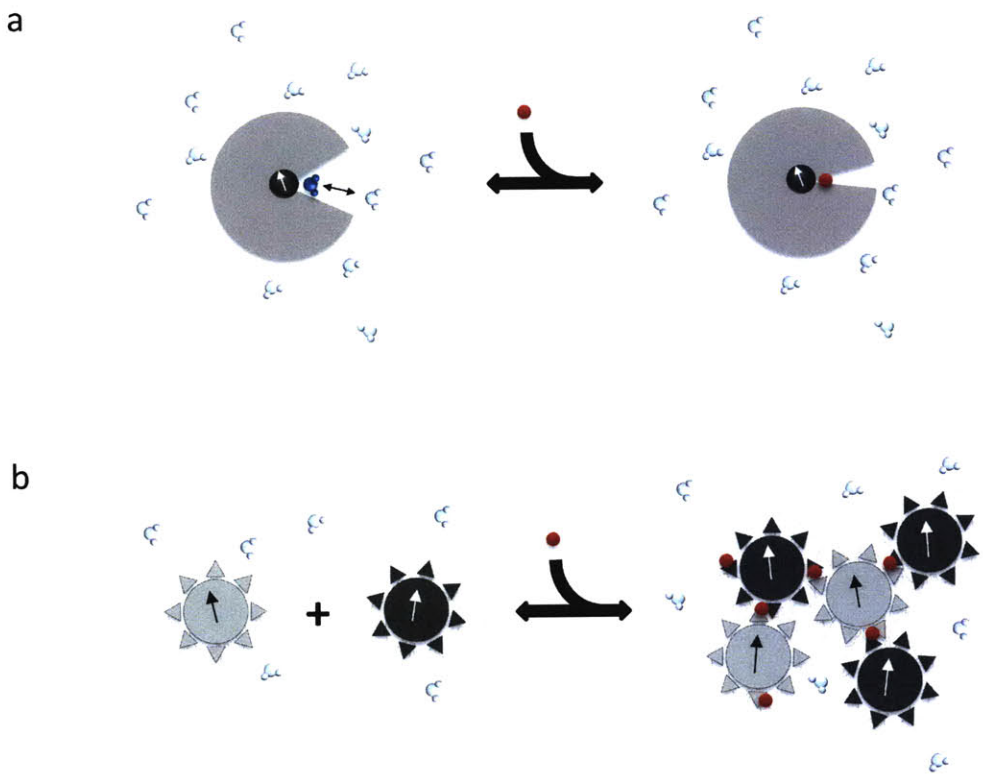

Figure 2. Device designs for MRI contrast sensors for soluble analytes. (a) Ligand (red) binding occludes water coordination at a paramagnetic ion, as in the cytochrome P450 BM3-based sensor reported by Shapiro et al. [50]. (b) Ligand (red) binding regulates clustering (aggregation) of superparamagnetic species in two populations, each carrying a binding parter whose interaction is ligand-dependent, as in the ferritin-based phosphorylation sensor reported by Shapiro et al. [51] and the functionalized nanoparticle-based calcium sensor reported by Atanasijevic et al. [45].

Only one metalloprotein with a reasonably strong T_2 relaxation effect has received substantial validation as an MRI contrast agent: the iron storage protein ferritin (Ft) [52,53,54]. Proteins in the ferritin family nucleate and catalyze the formation of a ferrihydrite species containing several thousand iron atoms in the core of a cage-like protein multimer [55]. Iron-loaded ferritin shows a surprisingly linear relationship between r_2 and applied magnetic field strength [56]. By analogy to the clustering-induced relaxivity enhancement observed for superparamagnetic nanoparticles [34], the observation that ferritin relaxivity in tissues is substantially higher than free suspensions of ferritin in solution has led to the hypothesis that tissue ferritin may be aggregated into clusters [57]. That possibility has already been exploited both to study the nature of ferritin's relaxation enhancement in tissues [57] and to

engineer a molecular fMRI sensor for protein phosphorylation [51], which will be discussed in greater detail in the next chapter (Figure 2b).

Accordingly, techniques from molecular biology and protein biochemistry present the opportunity to engineer arbitrary gains-of-function into natural metalloproteins. Based in on a theoretical understanding of NMR relaxation processes, we have introduced novel properties into natural metalloproteins to produce two platforms for developing molecular contrast sensors. The following chapters detail these efforts and their implications for molecular fMRI.

2 Design and demonstration of a genetically encodable T_2 MRI sensor for Ca^{2+} dynamics

2.1 Overview

Free calcium is a key intracellular second messenger in neural signaling, governing rapid presynaptic neurotransmitter release [58] as well as modulating cell state and synaptic plasticity [59]. In this work, we have undertaken the design and initial demonstration of a genetically-encoded molecular fMRI contrast sensor for Ca^{2+}. The sensor is an engineered two-component device that operates by reversible clustering of calmodulin-ferritin fusion proteins by a homotetrameric calmodulin-binding crosslinker based on DsRed. Calcium-dependent aggregation results in accelerated T_2 relaxation times *in vitro*. A preliminary investigation of sensor component expression in live mammalian cells is also presented.

2.2 Introduction

Diverse molecular events permit the propagation of information between neurons contacting one another at a synaptic cleft. As an action potential propagates down a presynaptic neuronal axon, the induced electrical potential across the axonal membrane causes voltage gated ion channels to open, allowing a rapid influx of Ca^{2+} down its concentration gradient into the cell. The transient rise in axonal free calcium precipitates a number of specific molecular events resulting in information propagation and signal modulation. Calcium mediates membrane fusion of intracellular presynaptic vesicles, releasing a burst of neurotransmitters into the extracellular matrix of the synaptic cleft [59].

Binding of neurotransmitters to specific receptors on the postsynaptic cell membrane transmits a signal into the downstream neuron [60]. The synthesis of information from binding events at numerous postsynaptic neurotransmitter receptors is integrated by an intracellular protein signaling network that serves to modulate the ionic, electrical, molecular, and expression state of the downstream neuron [61]. For example, some of these intracellular signaling events involve G-protein coupled neurotransmitter receptors (e.g. NMDA receptors for glutamate) containing cation channels, whose inward calcium ion flux is modulated by neurotransmitter binding as well as membrane potential and signaling pathway components [62]. This calcium flux may play a critical role in synaptic plasticity, the process by which neuronal cell-cell contacts are reorganized and strengthened in learning and memory [61].

Intracellular calcium dynamics therefore play an integral role in information propagation and processing in the brain. Several studies have demonstrated the tight temporal coupling between axonal calcium influx and action potential firing rates in a number of neuronal contexts [63,64,65]. We propose that calcium dynamics in the brain could be a direct signal of synaptic activity, one far closer molecularly, temporally, and spatially to transient electrical potentials than the BOLD effect (see Section 1.3) [2].

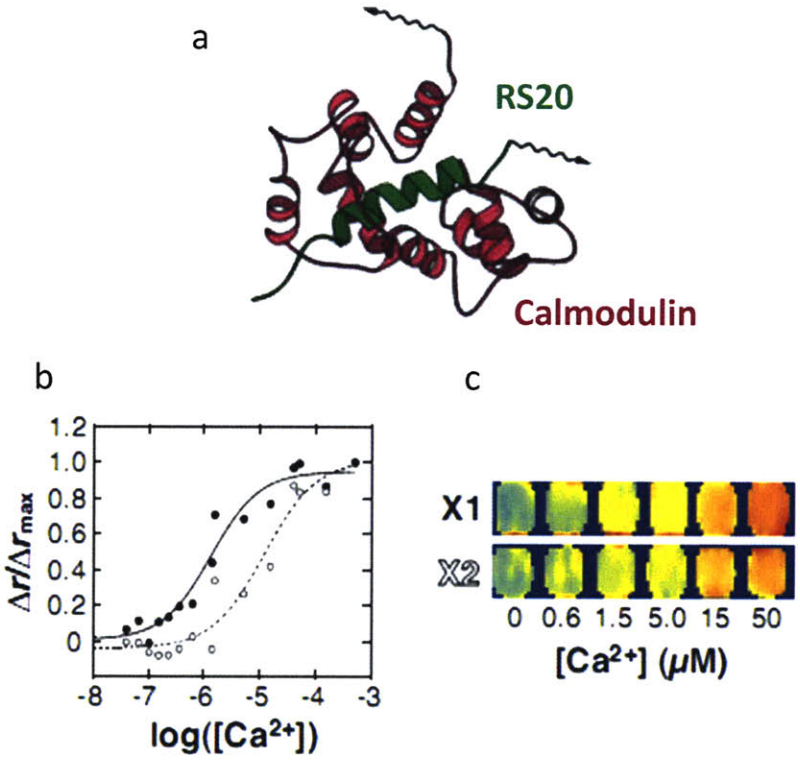

Figure 3. An aggregation-based contrast sensor for free calcium based on superparamagnetic nanoparticles reported by Atanasijevic et al.. Two species of iron oxide nanoparticles (diameter ≈ 50 nm) are synthesized with surface-immobilized calmodulin or a calmodulin-binding peptide, RS20, which interact in the presence of Ca^{2+}. (a) Ribbon diagram of the structural interaction between calcium-bound calmodulin (pink) and RS20 (green), derived from a crystal structure of the complex. (c) Calcium titration of aggregate size for sensors with immobilized Xenopus calmodulin mutants with two different calcium affinities, observed by a chance in transverse relaxivity. (d) T2-weighted MRI of the two sensors in (c) exposed to calcium at a range of concentrations. Red color indicates faster T2 relaxation rates, whereas blue color indicates slower rates. Adapted from [45].

To sense changes in free calcium levels, small molecule [66] and protein-based [47,67,68] fluorescent sensors for Ca^{2+} are already in widespread use. Meade and coworkers have demonstrated a synthetic T_1 contrast sensor, DOPTA-Gd, whose water coordination sites are exposed when chelating Ca^{2+} [41]. Interesting insights have also derived from the discovery by Koretsky and coworkers that paramagnetic Mn^{2+} could act as a Ca^{2+} analog and accumulate in highly active brain regions [36,37], although the kinetics of accumulation are generally too slow to observe dynamic processes of interest

[14]. However, for practical application, both of these methods T_1-based will require high concentrations (likely >10 μM) to accumulate at the site of interest.

Alternatively, inducible aggregation of paramagnetic nanoparticles at nanomolar concentrations enhances their T_2 relaxivity [43,69], and therefore calcium-inducible nanoparticle aggregation could be a practical mechanism to generate a sensor whose T_2 relaxivity varies with calcium concentration (Figure 2b). Atanasijevic et al. have recently demonstrated such an aggregation-based T_2 sensor for Ca^{2+} by mixing two populations of ~50 nm iron oxide nanoparticles, where each population displays either calmodulin (CaM) or calmodulin-binding peptides (CBP) on its surface (Figure 3) [45].

Practical application of such a multicomponent aggregation device *in vivo* would benefit from reengineering of the device for genetic encodability. Target cell machinery could supplant manual synthetic chemistry in producing the sensor, and genetic regulatory mechanisms could be tuned to directly govern desirable pharmacokinetics. Indeed, viral and transgenic methods to target specific cell types in the brain have been developed [11]. Furthermore, several genetically encoded calcium sensors based on fluorescent proteins have been demonstrated in live cells [47,67,70] and *in vivo* [68], taking advantage of the calcium-dependent interaction between CaM and a small alpha helical calmodulin binding domain, M13, to regulate the folding of a fluorescent protein or the Förster efficiency of energy transfer between two fluorescent proteins.

To produce genetically encodable paramagnetic nanoparticles, we turned to ferritins, a family of highly conserved cage-like protein complexes that sequester and oxidize free Fe^{2+}, and store iron in a hydrated iron oxide particle core [55]. Vertebrate ferritin is a 13 nm 24-subunit heteromultimer consisting of heavy (~21 kDa) and light (~19 kDa) chains whose relative stoichiometry vary in a species- and tissue-dependent manner [71]. Ferritin light chains (FTL) appear to nucleate the deposition of iron oxide grains in the form of ferrihydrite, with a variable stoichiometry often denoted as FeOOH. The iron

core tends to show asymmetrical geometry by TEM, with a maximal diameter of about 8nm containing up to ~4500 Fe atoms. Heavy chains (FTH) exhibit ferroxidase activity and appear to enhance the kinetics of deposition [72].

Iron-loaded ferritin is weakly paramagnetic at room temperature, exhibiting a T_2 relaxivity of about 0.8 mM^{-1} s^{-1} at 4.7 T [73]. Genove at al. have demonstrated that inducible ferritin overexpression from an adenoviral vector enhances T_2 contrast of both transformed human cells in culture and of adenovirally-infected mouse brain tissue *in vivo* [74]. Cohen et al. also recently reported tissue-specific inducible *in vivo* ferritin overexpression in transgenic mice and an associated acceleration in T_2 relaxation rates [52,53,74]. Furthermore, i*n vitro* aggregation of ferritin induced either by limited proteolysis [57] or chemical crosslinking [75] enhances T2 relaxivity of purified ferritin *in vitro*.

Shapiro et al. recently reported an MRI sensor based on phosphorylation-dependent aggregation and T_2 contrast enhancement of recombinant ferritin fusion proteins. Mixtures of two separately-prepared populations of modified ferritin heteromultimers could be induced to aggregate by PKA activity, where each population of ferritins incorporates human ferritin light chain (LF) fusions of either the PKA substrate domain KID or its cognate binding domain KIX [51]. Since the KID/KIX interaction is bimolecular, two otherwise identical ferritin fusions had to be produced, each carrying half of the molecular sensor—either KID or KIX (Figure 4a). For this reason, despite being genetically encoded, both components of Shapiro et al.'s kinase activity sensor cannot be productively encoded within the same cell. Simultaneous coexpression of these component subunits would result in a population of ferritins displaying both surface components (Figure 4b). Aggregation of such a species could be unreliable, since interactions between KID and KIX could be intramolecular upon phosphorylation.

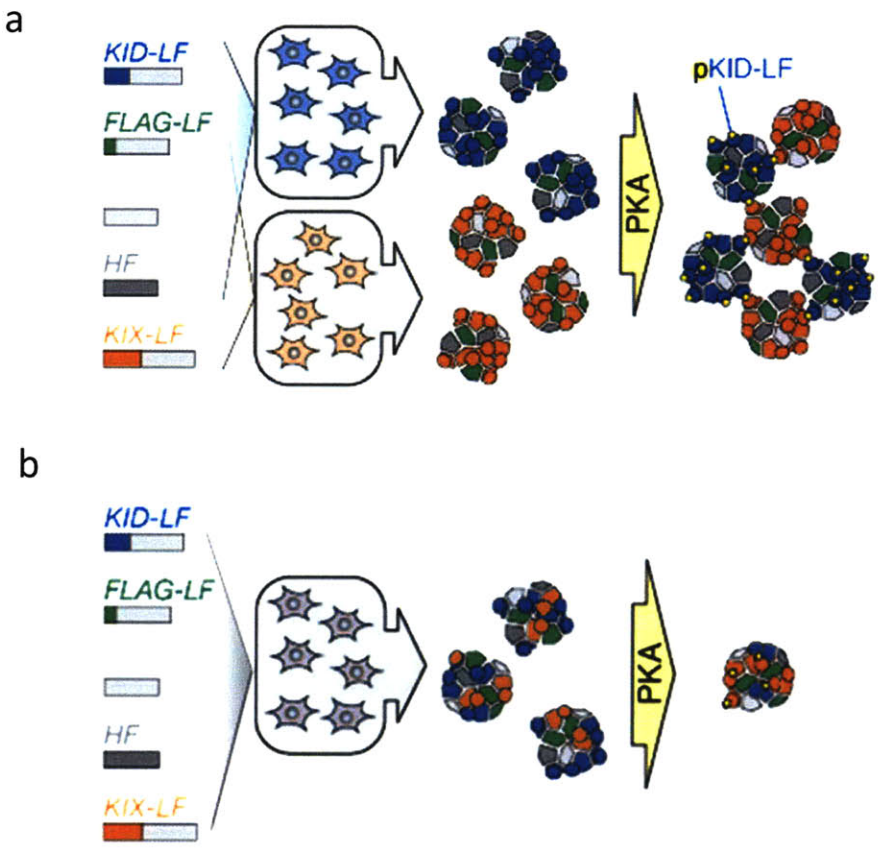

Figure 4. Design of a genetically-encoded contrast sensor for PKA phosphorylation activity based on ferritin. (a) Five constructs form the basis for the contrast sensor: PKA substrate KID fused to ferritin light chain (LF), FLAG-tagged LF for purification, untagged LF and ferritin heavy chain (HF), and the pKID-binding partner KIX fused to ferritin light chain. A subset of four constructs, with either KID-LF (blue) or KIX-LF (orange), were cotransfected into a population of HEK293 cells, and the separately purified recombinant proteins were mixed and assayed for phosphorylation-dependent aggregation. Adapted from [51]. (b) Thought experiment of the resultant mixed-KID/KIX sensor and unproductive phoshphorylation response if all five ferritin-based constructs were cotransfected into a single cell population.

Accordingly, we have built upon the design strategies of both the aforementioned nanoparticle-based Ca^{2+} sensor [45] and the genetically encodable ferritin-based kinase activity sensor [51] to produce a simplified aggregation device to sense intracellular Ca^{2+} levels by T_2-weighted MRI. In particular, we have introduced a novel "crosslinking" design strategy to allow all sensor components to be synthesized within the same cell.

2.3 Design

To sense Ca^{2+}, we took advantage of the interaction between calmodulin and a calmodulin-binding peptide, dubbed RS20, which derives from a regulatory domain of myosin light chain kinase (Figure 3a) [45]. It has been demonstrated with a modified version of the fluorescent Ca^{2+} sensor pericam that a free two component sensor based on such a calmodulin-peptide interaction can sense calcium in live cells, despite potential intracellular cross-reaction with endogenous calmodulin and calmodulin-binding domains [47]. As mentioned, Shapiro et al. also recently demonstrated that N-terminal fusions to human ferritin can operate as functional aggregation-based T_2 sensors [51].

To allow all sensor parts to be synthesized in the same cell, we designed a non-ferritin homomultimeric "crosslinker" that can inducibly aggregate a homogenous population of ferritins. As a homomultimeric carrier protein for RS20, we sought an obligate multimer with rich literature resources regarding stability, expression, and suitability for generation of fusion proteins. DsRed-Express is a red fluorescent protein variant derived from the coral *Discosoma sp.* that fits the aforementioned criteria. Many DsRed variants appear to be stable tetramers in solution [76,77] and have been crystallized as such [78]. Fusion proteins have been produced from DsRed-Express for use in culture and *in vivo* [79]. In the sensor presented here, RS20 has been fused to the C-terminus of DsRed-Express, connected by a short flexible linker sequence (See Methods).

Accordingly, we examined the viability of the device depicted in Figure 5, which consists of two components: (A) calmodulin-ferritin (CaM-Ft) fusion protein and (B) an RS20 homomultimer that could act as a crosslinker regulated by Ca^{2+} concentration.

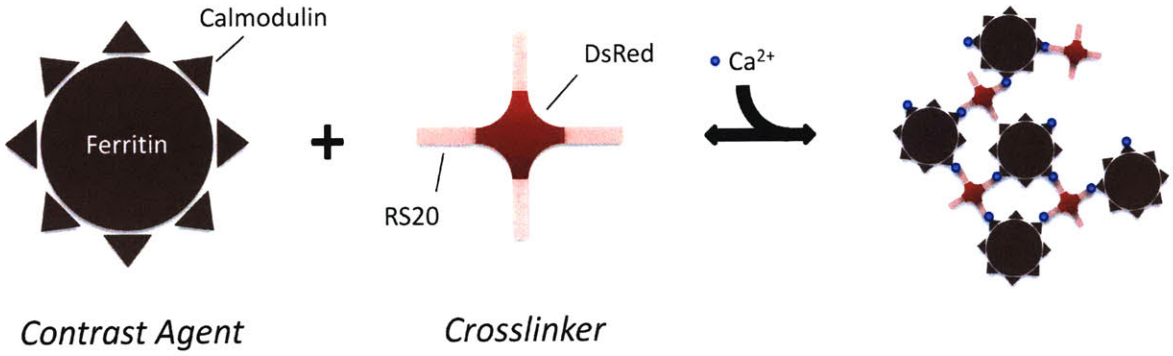

Figure 5. Design of a genetically encoded contrast sensor for free calcium based on crosslinkable ferritin. Calmodulin (CaM) fused to the N-terminus of ferritin (Ft) can be reversibly aggregated in a calcium-dependent manner by an engineered multivalent crosslinker consisting of homotetratmeric DsRed-Express fused to a calmodulin-binding domain, RS20.

2.4 Results

2.4.1 A calmodulin-ferritin fusion protein can be synthesized in E. coli when coexpressed with untagged heavy chains

A mammalian expression construct encoding a calmodulin-ferritin light chain fusion protein with a short intervening linker was generated by M. Shapiro in the course of his recent dissertation research, and this construct was generously contributed to the work presented here. It has been observed that homomultimeric heavy chain human ferritin (FtH) has ferroxidase activity [80] and may exhibit higher

iron loading than homomultimeric light chain human ferritin (FtL) [81]. A CaM-FtH fusion protein was therefore generated, as depicted in Figure 6, in order to compare the properties of FtH and FtL fusions.

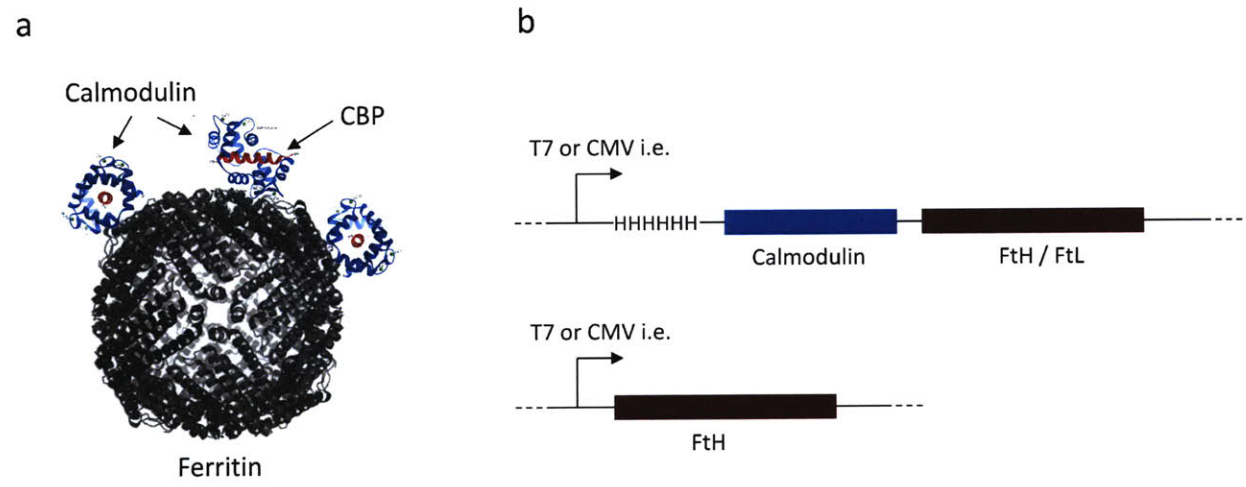

Figure 6. Design of a CaM-ferritin fusion protein and expression constructs. (a) Cartoon of the predicted structure of CaM-ferritin based on crystal structures of the two species, indicating the location of a calmodulin-binding peptide (CBP, red) that is similar to RS20 associated with calcium-bound CaM. (b) Cartoon of the bacterial and mammalian ferritin expression constructs generated in this work. CaM-FtH or CaM-FtL fusion proteins were generated with an N-terminal polyhistidine (His_6) purification tag, followed by Xenopus CaM and full length human FtH or FtL sequences described elsewhere [45,51]. Human FtH was also coexpressed in an untagged form during bacterial and mammalian expression. Expression was under the IPTG-inducible control of a LacI-repressed T7 polymerase promoter in bacterial constructs and under control of a strong constitutive cytomegalovirus (CMV) early-intermediate (i.e.) enhancer/promoter in mammalian constructs.

Since recombinant ferritins are expressible as soluble protein from *E. coli*, both bacterial and mammalian expression constructs were generated for N-terminally His_6-tagged CaM-FtH and CaM-FtL, as well as full length unmodified wildtype human FtH (see Methods). For bacterial constructs, a pET-based expression plasmid with an IPTG-inducible T7/lacI promoter/repressor system was constructed by standard methods. The CaM-FtH construct was then subcloned into a mammalian expression vector containing a cytomegalovirus (CMV) early/intermediate promoter-enhancer for high-level constitutive expression in mammalian cells. The CaM-FtH or the untagged FtH construct were inserted between the

CMV promoter and a downstream IRES site, which could drive bicistronic expression of neomycin, hygromycin, or puromycin selection cassettes for future stable transfection in mammalian cells).

For *in vitro* experiments, it was found that bacterially expressed ferritins could be rapidly loaded with iron in clarified lysate by a room-temperature titration in which drop-wise 100 mM ferrous ammonium sulfate was added until no color change was apparent while maintaining pH > 8.5 with drop-wise 1M sodium hydroxide. After overnight incubation at 4°C, neutralized lysate containing expressed ferritins composed of untagged FtH coexpressed with either His_6-CaM-FtH or His_6-CaM-FtL were purified by affinity chromatography using a standard procedure.

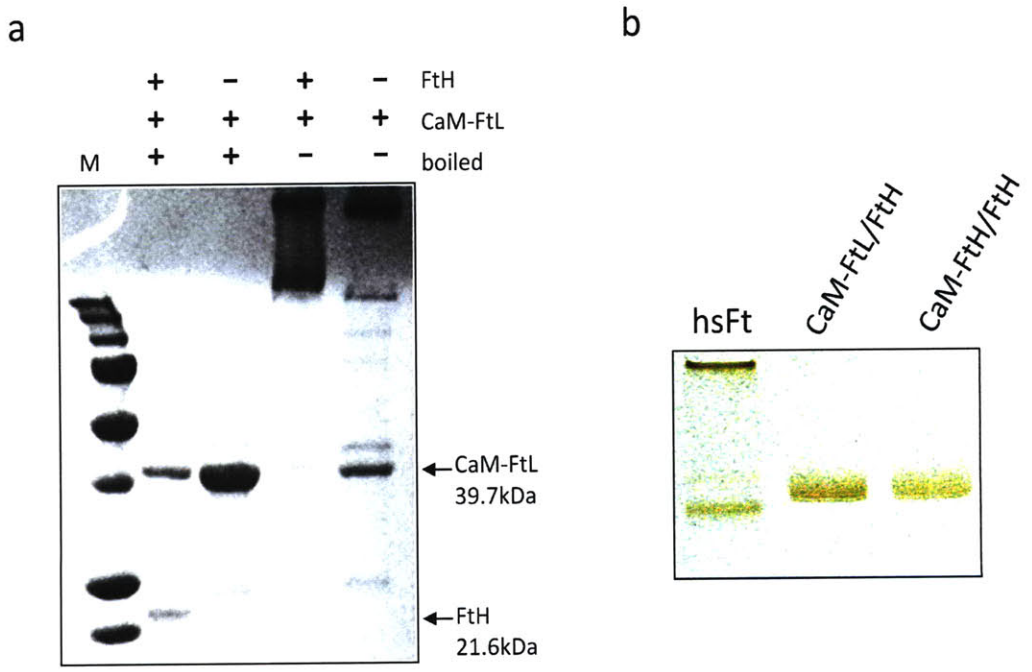

Figure 7. Recombinant CaM-ferritins can be bacterially expressed and migrate natively as a single species. (a) Purified proteins were separated by SDS-PAGE using a 4% stacking and 12% resolving gel and stained with Commassie Brilliant Blue G-250. Samples were boiled at 95°C for 10 min where indicated. (b) Expressed CaM-ferritins were loaded with iron in bacterial cell lysates with titrated ferrous ammonium sulfate (FAS), and the purifed ferritins and commercial horse spleen ferritin (hsFt) were separated on a native 7.5% PAGE gel in a 50 mM imidazole-HEPES pH 7.6 running buffer. The gel was photographed without staining.

The purified protein was separated by SDS-PAGE and visualized by Coomassie G-250 Brilliant Blue staining (Figure 7a). Since wildtype ferritin is relatively stable in SDS, unboiled samples show a high molecular weight smear (>>250kDa) of Coomassie stained material in the 4% polyacrylamide stacking layer that is too large to enter the 12% resolving layer (Lane 3). When samples are boiled in reducing SDS sample buffer, this high molecular weight material decomposes into two dominant bands corresponding to the predicted molecular weights of the CaM-Ft fusion protein (39.7 kDa for CaM-FtL and 40.9 kDa for CaM-FtH) and untagged FtH (21.6 kDa, Lane 1). In Figure 7a, it is also apparent that homomultimeric CaM-FtL alone shows lower SDS stability without coexpressed untagged FtH, since a nontrivial band of free CaM-FtL monomer is visible in the unboiled case (Lane 4). Finally, since ferritins are purified from lysate by affinity chromatography for the N-terminal polyhistidine tag of the CaM-Ft fusions, the appearance of a copurified band corresponding to the molecular weight of untagged FtH (21.6 kDa) indicates that native CaM-ferritins are properly a mixture of affinity tagged and untagged ferritin subunits at a ratio of 1.99:1 by densitometry (Lane 1).

The folding of heteromultimeric CaM-ferritins was assessed by separating purified CaM-FtH/FtH or CaM-FtL/FtH by native PAGE in a near-neutral (pH 7.6) running buffer and by directly observing the unstained native color of the ferritin iron core (Figure 7b). Both CaM-FtH/FtL and CaM-FtH/FtH run as single band toward the positive electrode, indicating that the species has an acidic isoelectric point and that ferritins are likely to be natively folded as an unsegregated species in solution.

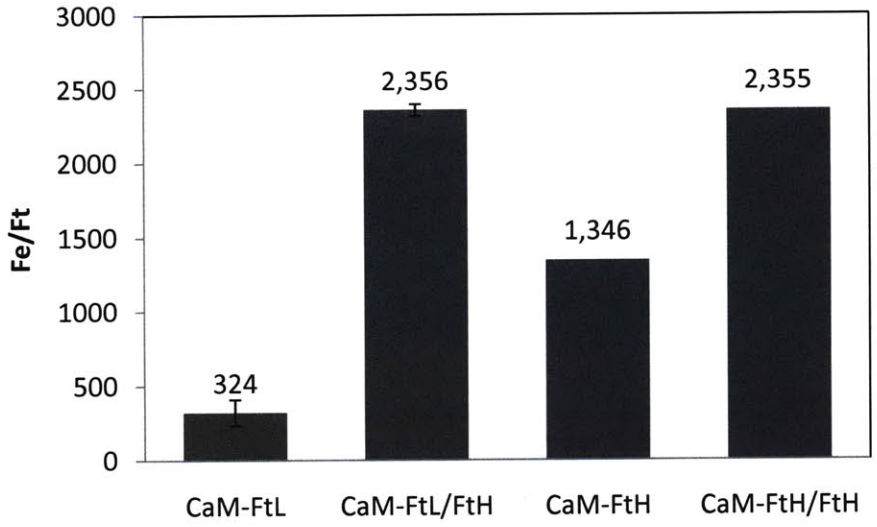

Figure 8. Bacterially expressed heteromultimeric CaM-ferritins consisting of untagged FtH show maximal iron loading. CaM-ferritins were loaded in lysate by titrating FAS and sodium hydroxide prior to Ni-NTA purification and gel filtration. Purified protein was quantified using protein assays, and iron content was quantified using the Fe(II)-chelating dye ferrozine in CaM-ferritin samples digested with sulfuric acid and reduced with thioglycolic acid. Error bars, where indicated, denote standard deviations of results from three independent preparations.

The extent of iron loading for heteromultimeric and homomultimeric CaM-ferritins was assayed colorimetrically with Fe(II)-binding dye ferrozine, following proteolytic hydrolysis and reductive solubilization of core iron. Given concentrations determined by colorimetric protein assays, we calculated that *in vitro* iron loading of heteromultimeric CaM-FtL/FtH and CaM-FtH/FtH were essentially equivalent at ~2400 atoms Fe/Ferritin, showing substantially improved iron loading compared to homomultimeric CaM-FtL or CaM-FtH alone (Figure 8). We opted to work primarily with CaM-FtH/FtH, since both heteromultimeric CaM-ferritins seemed biochemically equivalent based for our purposes.

2.4.2 A tetrameric DsRed-RS20 fusion protein can be synthesized in E. coli and self-associates

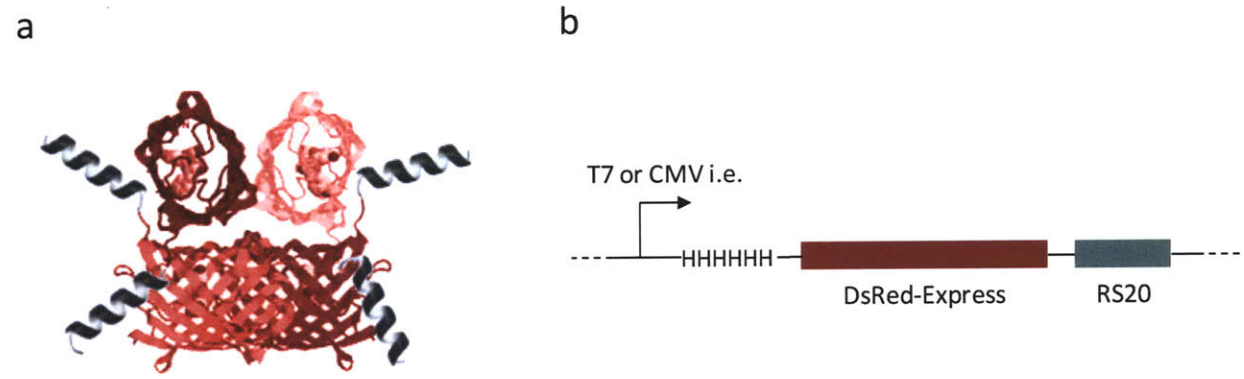

Figure 9. Design of a homotetrameric DsRed-RS20 fusion protein and expression constructs. (a) Cartoon of the predicted structure of DsRed-RS20 based on crystal structures of the two species, indicating homotetrameric DsRed in red and the RS20 calmodulin-binding domain in blue. (b) Cartoon of the bacterial and mammalian ferritin expression constructs generated in this work. DsRed-RS20 fusion proteins were generated with an N-terminal polyhistidine (His_6) purification tag, followed by DsRed-Express and the calmodulin-binding domain (RS20) derived from smooth muscle myosin light chain kinase [82]. Expression was under the IPTG-inducible control of a LacI-repressed T7 polymerase promoter in bacterial constructs and under control of a strong constitutive cytomegalovirus (CMV) early-intermediate (i.e.) enhancer/promoter in mammalian constructs.

The crosslinking component of the sensor is a DsRed variant C-terminal fused to the calmodulin-binding peptide RS20. To maximize expression in E. coli, this construct was based on RFP(EC2), an "*E. coli* optimized" variant of DsRed containing several mutations in the first nine amino acids, most of which are silent and are likely to improve ribosome binding site accessibility on transcripts in *E. coli* [83]. An N-terminal His_6 tag and a C-terminal RS20 sequence with codons optimized for both *E. coli* and mammalian expression were appended to full length RFP(EC2). As above, the construct was cloned in the context of a T7/lacI expression system for bacterial expression and then subcloned into a mammalian expression vector between a constitutive CMV early/intermediate promoter-enhancer and

a downstream internal ribosome entry site (IRES), followed by either neomycin or hygromycin selection cassettes (Figure 9).

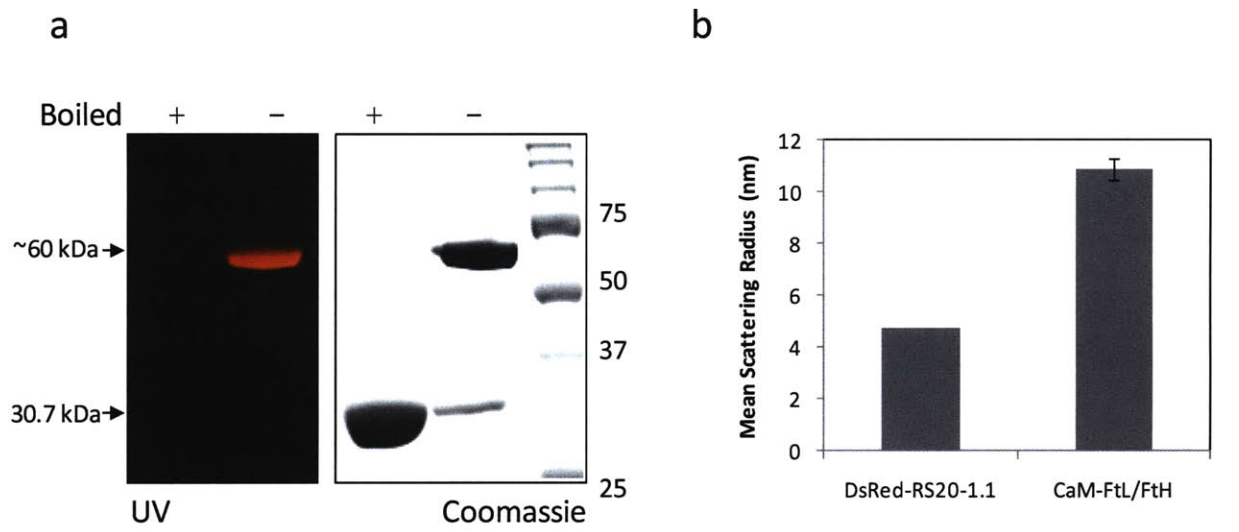

Figure 10. Recombinant DsRed-RS20 can be bacterially expressed and self-associates. (a) Expressed proteins were affinity purified and separated by SDS-PAGE using a 12% resolving gel, photographed under UV illumination (left) or stained with Commassie Brilliant Blue G-250 (right). Samples were boiled at 95˚C for 10 min where indicated. (b) Purified DsRed-RS20-1.1 (R17D linker mutant) appears tetrameric by DLS in HBS buffer. Error bars indicate standard deviations from three separate measurements.

Bacterially expressed DsRed-RS20 was purified from lysate under denaturing conditions. Unboiled and boiled samples of the purified protein were separated by SDS-PAGE, and the resulting gel displayed a band containing a red fluorescent species with an apparent molecular weight consistent with that of a dimer, 61 kDa, of the desired species (Figure 10). Upon boiling, the band denatures into a single nonfluorescent band whose migration is consistent with the 30.6 kDa calculated molecular weight for the desired DsRed-RS20 fusion protein in monomeric form. Finally, dynamic light scattering of the native protein reveals a hydrodynamic radius R_H = 4.76 ± 0.02 nm (mean ± S.D.) in HEPES buffered saline (HBS) which corresponds to a globular molecular weight of 129 kDa. This size is consistent with the predicted molecular weight, 123 kDa, of a species consisting of four 30.6 kDa monomers. We have

dubbed this engineered protein DsRed-RS20-1, to do denote the initial version of this tetrameric protein.

2.4.3 Recombinant sensor components reversibly aggregate and accelerate T2 relaxation as a function of calcium concentration, stoichiometry, and crosslinker pI

We sought to examine the behavior of mixtures of purified DsRed-RS20-1 and CaM-ferritin *in vitro* in the presence and absence of Ca^{2+}. All *in vitro* aggregation studies were done in a HEPES buffered saline and a low concentration of EDTA (500 μM) to chelate trace free calcium in the basal state. Several stoichiometric ratios of the interacting functional groups CaM:RS20 were examined for calcium-dependent aggregation both by dynamic light scattering (DLS) and T2-weighted MRI in the absence or presence of 500 μM $CaCl_2$. For DsRed-RS20-1 (Figure 11a), calcium-specific aggregation was observable when the CaM:RS20 ratio was 2:1, resulting in a 4.8-fold change in the mean hydrodynamic radius. Ratios showing maximal aggregation were also half-maximally (or worse) aggregated in the absence of calcium, suggesting that nonspecific hydrophobic or electrostatic interactions were dominating protein-protein contacts, especially when DsRed-RS20 was in excess.

After calculating the theoretical isoelectric points of the components (monomeric CaM-FtH pI = 4.9, FtH pI = 5.4, and DsRed-RS20-1 pI = 9.1), we hypothesized that electrostatics were playing a role in nonspecific aggregation. Accordingly, two charge mutants of DsRed-RS20-1 were generated, R17D (DsRed-RS20-1.1) and K249E (DsRed-RS20-1.2), with the goal of slightly lowering the pI of the fusion protein. A double mutant R17D/K249E was also generated (DsRed-RS20-1.3), but it was found to show

negligible improvements over the single mutants and was not scrutinized further (data not shown). These two mutations were targeted to domain linker regions not known to be functional in the sensor.

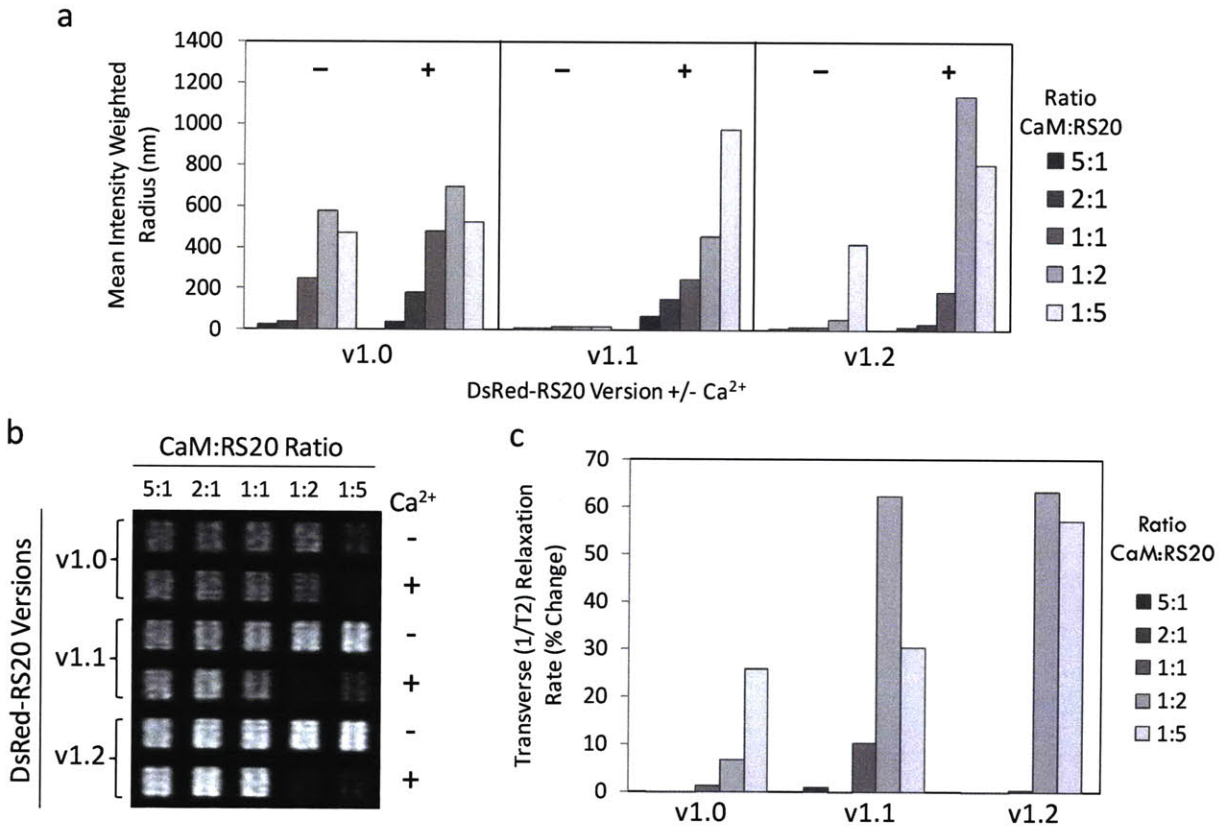

Figure 11. Calcium sensors aggregate and accelerate T_2 relaxation rates as a function of Ca^{2+}, stoichiometry, and isoelectric point. (a) Mean intensity weighted DLS radii of aggregates mixed at the indicated ratios of their functional groups, CaM and RS20, with or without 500 μM free Ca^{2+} (EDTA-buffered) in HBS (10 mM HEPES, pH 7.4, 150 mM NaCl, 500 μM EDTA). Version numbers refer to linker variants, where v1.1 and 1.2 have charge mutations R17D or K249E in the His_6-DsRed linker or DsRed-RS20 linker, respectively. CaM-FtH/FtH concentration is 1μM for all samples, as determined by a colorimetric protein assay. (b) T_2-weighted spin echo image of samples from (a) loaded into a 384-well microtiter plate and imaged with TE = 600 ms and TR = 4 s. (c) Quantification of relaxation rates fit from 30 echos with TE ranging from 20 ms to 600 ms in a single 1.63-mm slice through the multiwell plate at 4.7 T.

Mixtures of CaM-FtH/FtH with both charge mutants of DsRed-RS20 showed substantially reduced aggregation in the absence of calcium. For DsRed-RS20-1.1, mean radius fold change with calcium ($\overline{R_{H,Ca+}}/\overline{R_{H,Ca-}}$) was as high as 49-fold (973 nm with $CaCl_2$ vs. 19.9 nm without) at a 5-fold

excess of RS20 and 29-fold (454 nm vs. 15.9 nm) at 1:2 excess of R20 (Figure 11a). Both charge mutants exhibit robust aggregation upon incubation with calcium. However, the DsRed-RS20-1.1 mutant shows the best specificity across all tested stoichiometries of the two components. Uniquely, DsRed-RS20-1.1 even exhibits a 5-fold (68.7 nm vs. 13.4 nm) change when CaM is in 5-fold excess (5:1 CaM:RS20 ratio). DsRed-RS20-1.1's propensity to aggregate CaM-ferritins is therefore highly robust to the relative stoichiometry of the two sensor components. It is conceivable that this crosslinker variant's reduced electrostatic attraction to CaM-ferritin results in decreased avidity for intramolecular crosslinking when the crosslinker is no longer in excess.

For all three variants of the DsRed-RS20 crosslinker, we examined whether light scattering results are mirrored by a calcium-dependent change in contrast by T_2-weighted ^{1}H MRI of a multiwell plate filled with sensor mixtures in a range of relative stoichiometries of the two sensor components. A single T_2-weighted spin-echo intensity image at TE = 600 ms and TR = 4000ms shows a dramatic contrast difference between calcium-treated and untreated samples (Figure 11b). Relaxation time constants (1/T2) were fit from the signal intensities obtained from 30 echoes (TE = 20 ms intervals, TR = 4000 ms) in a multi spin multi echo (MSME) pulse sequence at 4.7 T in a single 1.63 mm slice across the multiwell plate. The percent change in relaxation time constant between the calcium-negative and calcium-positive (Figure 11c) was maximal at 26% for DsRed-RS20-1 at a CaM:RS20 ratio of 1:5, whereas signal change was maximal at a ratio of 1:2 for the charge mutants DsRed-RS20-1.1 (62%) and DsRed-RS20-1.2 (63%). It is worth noting that some trends do not match precisely between the scattering data and T_2 relaxometry. For example, DsRed-RS20-1.1 incubated at a 1:5 ratio shows the largest aggregates by DLS, but apparently shows T_2 brightening (lower r_2) by MRI. This observation would be consistent with aggregation beyond the static dephasing limit into an echo time-limited "slow motion regime," such that further increases in the diffusional correlation time, τ_D, result in decreases in r_2 [44].

Kinetics and reversibility of calcium-dependent DsRed-RS20-1.1/CaM-Ft aggregation were examined under nonequilibrium conditions (Figure 12). Calcium or EDTA solutions were added where indicated, and the scattering intensity and fit radius were monitored over time. Aggregation was found to be rapid, reaching equilibrium scattering intensity on a timescale of approximately two minutes for micromolar concentrations, while higher calcium concentrations induced faster aggregation, as expected. Disaggregation appeared to be nearly instantaneous within the resolution of this experiment on treatment with the chelator EDTA.

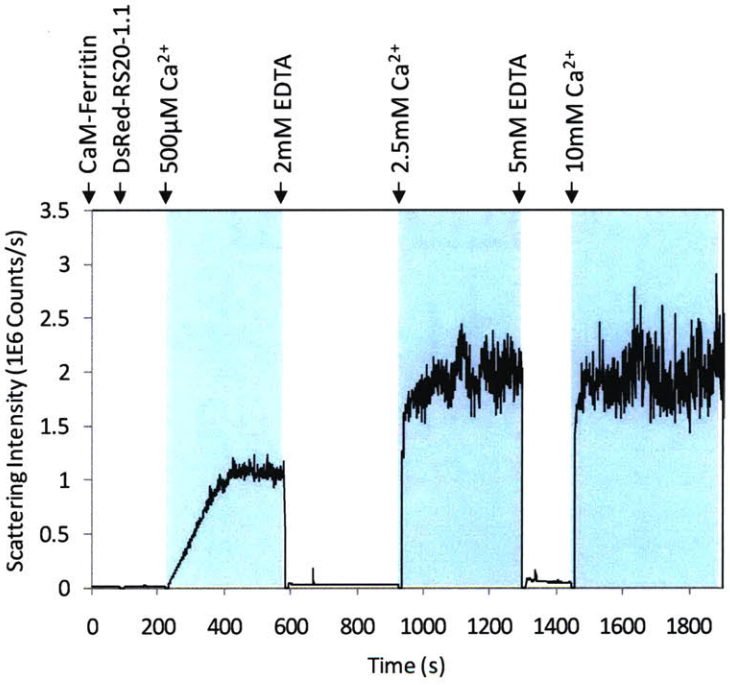

Figure 12. Calcium sensor aggregation is rapid and reversible. Species were added to 1 μm CaM-ferritin in HBS buffer at the indicated times and DLS scattering intensity was monitored continuously. DsRed-RS20-v1.1 crosslinker was added at t = ~95 s in a ~1:2 CaM:RS20 ratio. Blue-background regions indicate when Ca^{2+} is in excess over EDTA.

Since it showed the best aggregation characteristics of the three variants we examined, we chose to focus on the DsRed-RS20-1.1 variant as the crosslinking component of our sensor. Accordingly,

the sensor described from here onwards consists of the components in Table 1, except where otherwise indicated.

2.4.4 *DsRed-RS20-1.1 crosslinker-mediated CaM-ferritin aggregation is robust to the presence of detergent-free cell lysate* in vitro.

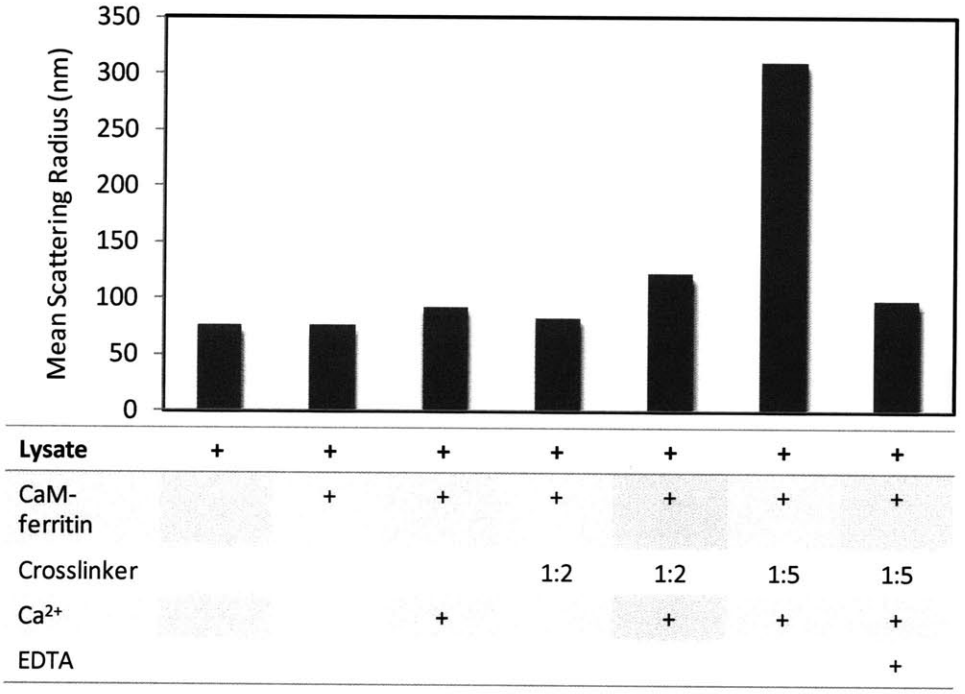

Figure 13. Calcium sensors aggregate in the presence of 293 cell lysate as a function of Ca^{2+} and component stoichiometry. Mean intensity weighted DLS radii of aggregates mixed at the indicated ratios of their functional groups, CaM and RS20, with or without 500 μM free Ca^{2+} (EDTA-buffered) in HBS. Version numbers refer to linker variants, where v1.1 and 1.2 have charge mutations R17D or K249E in the His_6-DsRed linker or DsRed-RS20 linker, respectively. CaM-FtH/FtH and 293 cell lysate concentrations were1μM and ~10 mg/mL, respectively, for all samples, as determined by a colorimetric protein assay.

To probe whether intracellular proteins might disrupt sensor function in cell cytosol, we examined the effect of adding detergent-free mammalian cell lysate to the aggregation reactions

detailed in Section 2.4.4 (Figure 13). Transformed human embryonic kidney cells (HEK293H) were lysed by repeated freeze-thawing, clarified, and filtered to eliminate large protein complexes that would interfere with scattering measurements. The filtered lysate at ~10 mg/mL alone showed a mean R_H = 76 nm in the presence of 100 μM EDTA, and this background size did not increase substantially on addition of CaM-ferritin, CaM-ferritin with 1 mM calcium, or CaM-ferritin with DsRed-RS20-1.1 (CaM:RS20 = 1:2) in the absence of calcium. Mixtures of all sensor components in the presence of lysate and calcium, however, showed increases in mean radius to 122 nm (1:2) and 311 nm (1:5), which appeared to disaggregate upon treatment with EDTA.

Component	Function	N-Terminus	C-Terminus	Multivalency	Multimerization
CaM-ferritin	T2 Contrast, Ca^{2+} Sensing	Calmodulin	H-Chain Ferritin (FtH)	~14	Hetero (with untagged H-chain)
DsRed-RS20-v1.1	Crosslinker	DsRed-Express	RS20	4	Homo

Table 1. Engineered components of a T_2 calcium sensor.

2.4.5 CaM-FtH/FtH expression accelerates T_2 relaxation rates of transiently transfected human lung adenocarcinoma cells

To begin assessing the viability of intracellular expression of sensor components, constructs for CaM-FtH, untagged FtH, and DsRed-RS20-1.1 were subcloned into mammalian expression vectors. T2 contrast enhancement from overexpressed ferritin in cultured human lung adenocarcinoma A549 cells

has recently been reported [74]. In this work, the authors found that ferritin overexpression conferred a significant contrast enhancement only after media supplementation with the Fe(III) source ferric ammonium citrate (FAC). This result suggests that iron uptake by A549 cells is sufficient to load a quantity of iron into overexpressed ferritin, although a precise quantification of ferritin iron saturation was not undertaken by the authors.

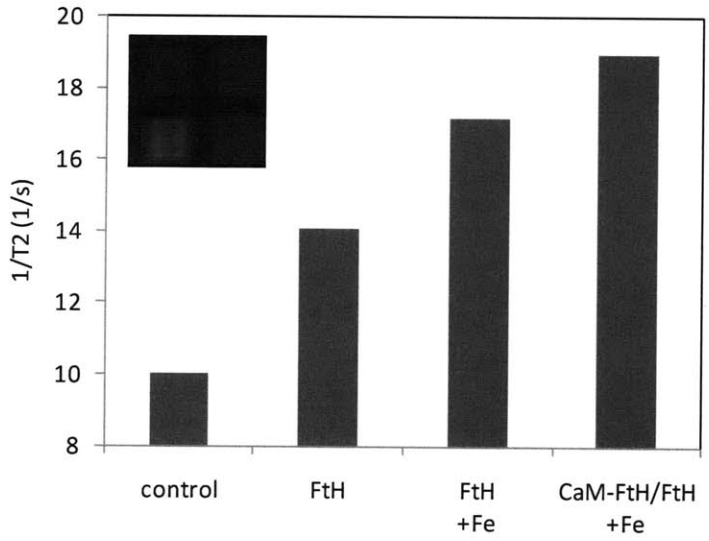

Figure 14. Transiently transfected A549 lung adenocarcinoma cells express recombinant CaM-ferritin and exhibit accelerated T2 relaxation rates. Transverse (1/T2) relaxation rates of pelleted A549 cells washed in HBSS 48 hr after transiently transfection with FtH alone or cotransfected with CaM-FtH/FtH. Cell medium was supplemented with 100 μM ferric ammonium citrate (FAC) and 100 mg/mL holotransferrin where indicated. Inset: T2-weighted MRI intensity image of a 1.63-mm slice across the multiwell plate at 4.7 T, TR = 4 s, TE = 140 ms (bottom-left: untransfected control, bottom-right: unsupplemented FtH transfected, top-right: Fe-supplemented FtH, top-left: Fe-supplemented CaM-FtH/FtH).

We have therefore examined the effects of increased Fe(III) in the culture medium of ferritin-expressing transiently transfected A549 cells. Cells were transfected briefly (2 h) with constitutive CMV promoter constructs encoding CaM-FtH/FtH or FtH alone and then incubated for 48 h in iron-rich complete medium (see Methods) where indicated (Figure 14) [84]. Harvested cells were washed extensively, pelleted in a 384 well plate, and imaged by a T_2-weighted spin echo pulse sequence.

Transfection with FtH alone in medium containing 10% serum was sufficient to confer T_2 shortening, although FtH-overexpressing cells treated with iron supplements show substantially faster relaxation times, as in [74]. Interestingly, coexpression of CaM-FtH and unlabeled FtH appears to result in higher T_2 enhancement than FtH alone. One might speculate that differences in subcellular compartmentalization or expression levels may contribute to this effect. At a minimum, the CaM-FtH fusion protein does not negatively interfere with iron uptake in A549 cells.

2.4.6 Cells transiently transfected with the sensor show a change in subcellular fluorescence localization on treatment with a calcium ionophore

Transient transfection of A549 cells with a constitutive construct encoding DsRed-RS20-1.1 resulted in strong intracellular red fluorescence. After 24 – 48 hours post-transfection, fluorescence appears in both the cytosol and nucleus, with somewhat stronger nuclear signal in cells co-transfected with CaM-FtH/FtH (Figure 15, t = 0), although heterogeneity in subcellular localization was apparent across the dish (data not shown). Strong fluorescence signal can be observed in a small number of punctate cytoplasmic bodies and possibly in nucleoli. Some cells show generally diffuse localization, with a strong fluorescence signal and poor cell morphology (data not shown). This population heterogeneity may be due to differences in transfection complex loading, an effect of transfection toxicity, or cell cycle differences. Generally, cells with intermediate and lower fluorescence intensity showed normal cell morphology.

In vitro, we observed that calcium-dependent aggregation had no effect on observable red fluorescence of the sensor for three DsRed-RS20-1 variants across a range of stoichiometries in HBS

buffer (data not shown), perhaps because aggregates are too amorphous for self-quenching or FRET quenching effects. On treatment with calcium ionophore ionomycin in the presence of high extracellular Ca^{2+} [85], cells showed a change in subcellular localization of fluorescence that was different between those expressing DsRed-RS20-1.1 alone and those co-expressing CaM-FtH/FtH (Figure 15). Specifically, ionomycin treatment

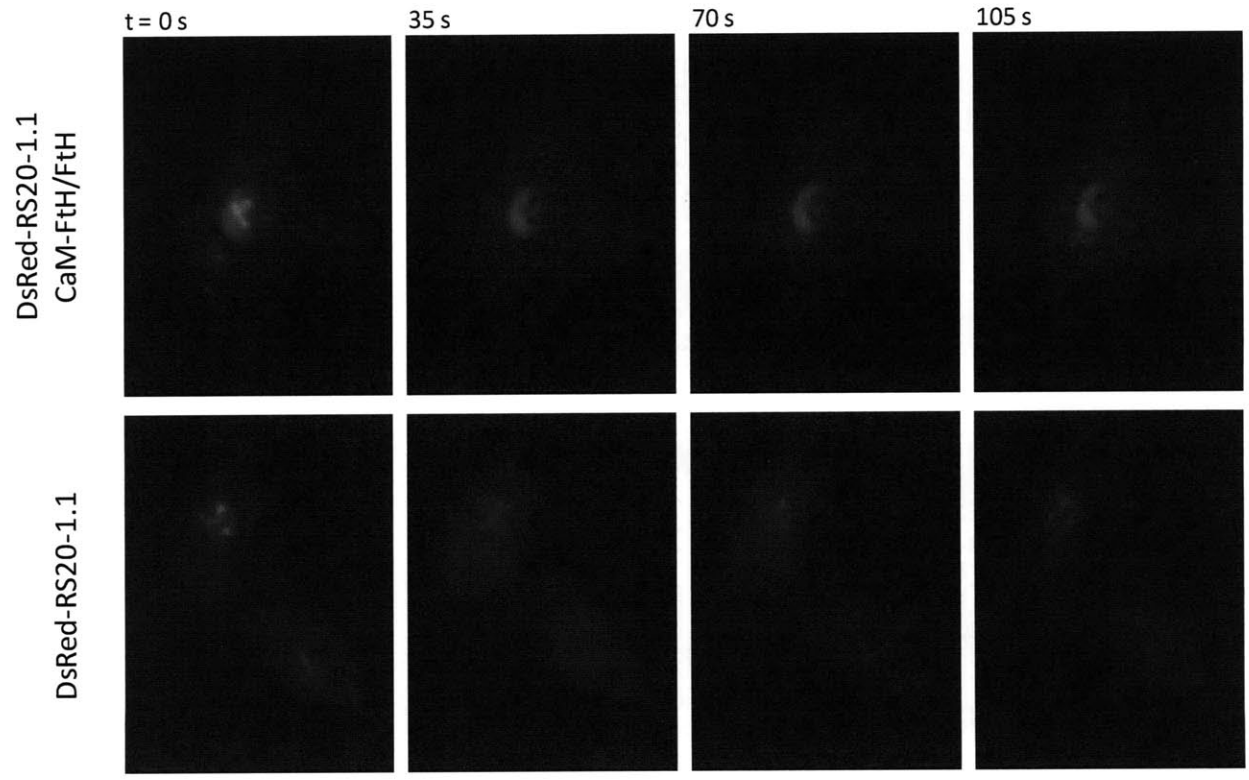

Figure 15. Subcellular localization of DsRed-RS20-1.1 fluorescence is altered by ionomycin treatment in live transiently transfected A549 lung adenocarcinoma cells with and without co-transfected CaM-FtH/FtH. A549 cells were transfected with constitutive DsRed-RS20-1.1 alone (bottom) or with CaM-FtH and FtH constructs (top) for 24 h washed and imaged in HBSS containing ~11 mM $CaCl_2$ and 1mM $MgCl_2$. At t = 0, live cells were treated with 2.5 μM ionomycin, a calcium ionophore that chelates and shuttles Ca^{2+} across membranes. Imaging was performed on a compound fluorescence microscope equipped with a xenon lamp and CCD camera.

2.5 Discussion and Conclusions

In this chapter, I have described an engineered device to sense calcium levels that has been developed and demonstrated *in vitro*. The novel contrast agent "crosslinking" design strategy employed here should be generalizable for making aggregation-based MRI sensors based on any two-component ligand-inducible protein-protein interaction. Use of such a crosslinker might substantially reduce the synthetic complexity of sensors based on of superparamagnetic nanoparticles, such as those presented in Atanasijevic et al.'s calcium sensor.

Having hypothesized that electrostatics play an important role in the sensor's aggregation specificity, we made rational mutations that resulted in sensor variants that show dramatically low nonspecific aggregation in the absence of calcium while retaining a significant aggregation response in the presence of calcium. Aggregation kinetics observed for this sensor variant are sufficiently rapid to observe calcium dynamics on a timescale of minutes. Initial testing in detergent-free mammalian cell lysate suggests that intracellular function is plausible in the context of cell proteins, and preliminary observations of DsRed-RS20-1.1 fluorescence suggest that an intracellular clustering may occur as a response to ionophore-induced intracellular calcium influx.

It is worth noting, however, that while calcium-dependent sensor aggregation was robust to the presence of cell lysate, mean radii in Figure 12 were somewhat lower for a given CaM:RS20 ratio in the presence of detergent-free lysate than observed in the absence of lysate. This suggests that endogenous cellular components do compete for the CaM-ferritin and DsRed-RS20-1.1 binding sites, either by specific or nonspecific interactions. However, since the aggregation effect appeared

recoverable when RS20 sites were in higher excess, it is likely that appropriate sensor function can be achieved intracellularly by tuning DsRed-RS20-1.1 expression to an appropriate excess over CaM-ferritin. Similarly, Miywaki et al. found that the FRET-based calcium sensor YC2.1 had markedly increased interaction with free CaM compared to sensors consisting of both CaM and M13, a calmodulin binding peptide similar to RS20. The authors further hinted at a change in subcellular localization of the split sensor components upon increases in intracellular calcium [86], an observation that we have also made with transiently transfected DsRed-RS20-1.1 (data not shown).

Specific interactions with endogenous CaM or CaM-binding proteins may also interfere with normal cellular function. Further work is necessary to demonstrate the viability of this sensor in an intracellular context and to tweak the design to overcome likely challenges. For example, mammalian expression constructs have been generated and confer heterogeneous expression in transiently transfected cells, but it was not possible to select stable integrated clones from this population. We hypothesize that the expression levels of this initial CMV promoter construct could be too high for selection, perhaps due to off-target effects on calcium-regulated processes involved in growth. This explanation is conceivable in our present design, in which Xenopus calmodulin and MLCK calmodulin binding domains are incorporated into the two components of the sensor, and it is compatible with the observation that aggregates are smaller in detergent-free cell lysate for a given relative stoichiometry of sensor components. However, we believe these challenges can be overcome using a weaker or inducible promoter system or through either a rational or a screening approach to generate calmodulin and RS20 variants that have orthogonal binding specificity [87,88].

Ideally, an expression system should be developed to stably express the ferritin component in tissue culture cells and, ultimately, *in vivo*. While the DsRed-RS20 crosslinking component could imaginably be induced when necessary, the utility of the sensor relies critically on the kinetics of iron

loading into CaM-ferritins. A rapid system to manifest iron loading is conceivable in tissue culture, e.g. by manipulating cellular iron uptake. On the other hand, it will be challenging to manipulate *in vivo* iron bioavailability in practical experimental contexts. It seems more plausible that stable constitutive expression of sensor components over an extended period of time (e.g. using genome-integrating viral vectors or transgenic animals) could permit sufficient iron loading into overexpressed ferritin.

Since others have observed contrast effects of overexpressed ferritin using inducible expression systems in cultured cells and *in vivo* [52,53,74], and since we have also demonstrated iron loading of transiently transfected CaM-ferritin in cultured cells, we are optimistic that a functional CaM-ferritin contrast agent could be viably expressed *in vivo*. Also, we observe robust expression arising from pilot experiments with transiently transfected DsRed-RS20 in cultured cells. Accordingly, we believe that adaptation of the all parts of the calcium sensor system for simultaneous expression in tissue culture cells will be viable in the near future. Further work to assess sensitivity to intracellular calcium dynamics could then proceed in the desired intracellular context.

2.6 Materials and Methods

2.6.1 Cloning of DsRed-RS20 and CaM-ferritin fusion proteins

Full length human ferritin heavy chain (FtH) and light chain (FtL) were initially cloned into pCMV-Sport vectors as previously described [45]. Xenopus calmodulin (CaM) was fused N-terminally to FtL with an intervening GTSSEF linker sequence and was generously provided by Mikhail Shapiro. For IPTG-

inducible bacterial protein expression, CaM-FtL was subcloned into the NdeI/XhoI sites of pET28a (Novagen), resulting in an N-terminally His_6-tagged construct. CaM-FtH was assembled by excising the EcoRI/XhoI fragment containing FtL and religating the purified backbone with the corresponding EcoRI/XhoI fragment from pCMV-Sport-FtH containing full length FtH. FtH was also subcloned for bacterial expression by excising an NcoI/XhoI fragment from pCMV-Sport-FtH and ligating the fragment into NcoI/XhoI digested pET16b. CaM-FtH and untagged FtH constructs were NcoI/XhoI sites further subcloned into mammalian expression vectors pTriEx3-hyg (Novagen) and pIRESpuro3 (Clontech), respectively. All clone selection was performed by transforming ligations into chemically competent DH5α T_1^R *E. coli* (Invitrogen) and plating on selective media. DNA isolated from single clones was sequenced to verify the construct using a T7 promoter primer (New England Biolabs).

DsRed-RS20 was constructed using the sequence RFP(EC2) produced in the Keasling laboratory for improved bacterial expression of DsRed proteins [83]. This variant of DsRed-Express contains several silent mutations in codons 2-4 that the authors suggest may improve translation efficiency. Full length RFP(EC2) was cloned as an N-terminal fusion to a codon optimized sequence encoding the myosin light chain kinase (MLCK) calmodulin binding peptide RS20 [45] with an intervening linker sequence GSSKGG. This fusion was inserted between the NdeI/XhoI sites of pET28a, resulting in an N-terminal His_6-tagged construct under the control of a T7/lacI promoter/repressor system. The linker between the His_6 purification tag and DsRed contains a thrombin protease recognition site (SSGLVPRGSH). An arginine in this site was mutated to aspartic acid (R17D) using site directed mutagenesis (Quikchange, Stratagene) to reduce the predicted isoelectric point of the fusion protein, and this variant was designated DsRed-RS20-1.1. Another charge mutant was also generated (K249E), DsRed-RS20-1.2, which replaces a lysine in the linker sequence between DsRed and RS20, resulting in the linker (GSSEGG). Finally, a fusion protein with the two domains in reverse order (N-terminal RS20-DsRed) was produced, but it was found to have poor expression in *E. coli* (data not shown). For mammalian expression, an NcoI/XhoI fragment

containing DsRed-RS20(R17D) was subcloned into pTriEx3-neo (Novagen). All constructs were verified by restriction digest and sequencing using a T7 promoter primer.

2.6.2 Recombinant protein expression and purification

Sensor components for *in vitro* assays were synthesized recombinantly in *E. coli*. Chemically competent BL21(DE3) pLysS cells (Invitrogen) were cotransformed with constructs encoding FtH and either CaM-FtL or CaM-FtH. Cotransformants were selected for growth on LB agar containing 50 μg/mL kanamycin and 100 μg/mL ampicillin. Liquid LB cultures were grown to mid-log phase and induced by addition of 1 mM IPTG for 4 hours at 30C. pET28-DsRed-RS20 constructs were transformed into BL21(DE3) Star (Invitrogen) *E. coli*, and cultures were grown using the same procedure, except induction proceeded overnight at 30°C.

Induced cultures of DsRed-RS20 proteins were harvested by centrifugation. The highest protein yield was observed when lysated were generated under denaturing conditions using the Pierce Inclusion Body Solubilization Reagent, clarified by centrifugation at 16,000 g, and incubated for 2 h at 4°C with Ni-NTA Superflow agarose resin (Qiagen). The resin was then loaded into an empty gravity column and washed with two column volumes of the solubiliztion reagent, followed by 20 column volumes of a native wash buffer containing 20 mM imidazole, 50 mM sodium phosphate, pH 8.0, and 300 mM NaCl. The protein was then eluted in the same buffer containing 250 mM imidazole and desalted by gel filtration using a PD10 G-25 Sephadex (GE Amersham) disposable column equilibrated in 10mM HEPES, pH 7.4 with KOH, and 150mM NaCl. Purity was analyzed by SDS-PAGE of boiled or unboiled samples.

Induced cultures of expressed CaM-ferritins were harvested and lysed using a Bugbuster lysis reagent containing lysozyme and benzonase (Novagen) as per the manufacturers' instructions, with the addition of an EDTA-free protease inhibitor cocktail at a 1:1000 dilution (EMD Biosciences). Induced lysates containing ferritin generally show negligible insoluble matter, and therefore clarification is often unnecessary. Purification proceeded after titrating 100mM ferrous ammonium sulfate drip-wise until no further color change was observed. Solution pH was maintained >8.5 using 1M NaOH. Lysates were agitated overnight at 4°C and then purified using Ni-NTA agarose resin, as above. Purity was analyzed by SDS-PAGE separation with Coomassie Brilliant Blue G-250 staining with or without boiling for 10 min at 95°C in reducing sample buffer. Proper folding of purified ferritin proteins was assayed by native PAGE in a 50mM imidazole-HEPES running buffer, pH 7.5, and iron-loaded ferritin was visualized by its native coloring under white light.

Protein concentrations were determined with a bicinchoninc acid (BCA) assay or Pierce 660nm Protein Assay using either BSA or horse spleen apoferritin (Sigma) as a loading control. Iron loading was assayed by digesting protein samples at a range of dilutions in H_2SO_4 and reducing Fe(III) to Fe(II) using thioglycolic acid (TGA). Iron concentration was assayed colorimetrically with the Fe-chelating dye ferrozine (Sigma). For example, 10µL of protein solution was mixed with 20µL 2M H_2SO_4 and 20uL concentrated TGA (Sigma) and incubated at room temperature for 30 minutes. Solutions were neutralized by addition of 40µL 2.5 M sodium acetate and incubated with 20µL 0.1M ferrozine for 30 minutes further. Samples were then diluted by addition of 750µL ultrapure water and absorbance at 562 nm was read on a UV/Vis spectrophotometer. Fe(II) concentrations were calculated using the ferrozine-Fe(II) molar extinction coefficient ε_{562nm} = 29,700 M^{-1} cm^{-1} [89].

2.6.3 Dynamic light scattering (DLS)

Light scattering experiments were performed on a Dynapro DLS system (Wyatt Technologies) equipped with a temperature controlled cuvette holder maintained at 37°C. All measurements were performed in HEPES-buffered saline (HBS): 10 mM HEPES, 150 mM NaCl, 0.5 mM EDTA, adjusted to pH 7.4 with KOH. Buffers and purified protein samples were prefiltered using 0.2 micron syringe or centrifugal filters. Mixed samples were loaded into a quartz cuvette which was then equilibrated at the set temperature for two minutes prior to data collection. To assess equilibrium aggregation state, 10 acquisitions were collected per second for 50 seconds. The manufacturer's software Dynapro reported a fit mean intensity-weighted hydrodynamic radius, *R*, by fitting to an isotropic sphere model. For non-equilibirum kinetics experiments, filtered $CaCl_2$ or EDTA stock solutions were diluted into mixed protein samples at indicated intervals, and the solution was quickly mixed by rapid aspiration and expulsion during the course of uninterrupted acquisition at 1-sec intervals. Note that scattering and transmission detectors are swamped by external lighting for several seconds while the cuvette door is open during this process, and therefore no scattering appears during this short interval.

2.6.4 MRI relaxometry

Protein samples at a range of relative stoichiometries were diluted in 0.2 micron filtered HBS buffer into 384-well microtiter plate wells (BD Falcon), and peripheral plate wells were filled with buffer alone. Where indicated, deionized water or 1 mM filtered $CaCl_2$ was added such that its final concentration was approximately 500 μM, buffered by EDTA. The plate was imaged at room

temperature in a 4.7 T Bruker Avance animal scanner with a 40cm-bore. Images were taken in a 1.63-mm slice across the plate using a multi-spin multi-echo (MSME) pulse sequence with the following parameters. Time to echo (TE) ranged from 20 - 600 ms in 20 ms increments for 30 echoes. Repetition time (TR) was 4000 ms. Four scans were taken and averaged. T_2 relaxation rates were fit from reconstructed image data using custom routines developed in Matlab (Mathworks).

2.6.5 Mammalian tissue culture, transfection, and ionomycin treatment

Human lung adenocarcinoma A549 cells (ATCC) were cultured at 5% CO_2 and 37°C as recommended by the supplier in Kaighn's F-12K medium (Invitrogen) containing 10% fetal bovine serum and typical penicillin and streptomycin antibiotics. At 90-95% confluence, cultures were washed and preincubated for 30-60 min in OptimMEM-1 medium (Invitrogen), followed by transfection with Lipofectamine 2000 (Invitrogen) by the manufacturer's protocol. After 1.5 – 2 hours, OptiMEM and transfection complexes were aspirated and replaced with fresh complete growth medium and, where indicated, 100 μM filter sterilized ferric ammonium citrate. Transfected cells were incubated for a further 24 – 48 hours prior to microscopy or MRI experiments. Fluorescence microscopy was performed on cells washed twice in Hank's Balanced Salt Solution (HBSS) containing 1 mM $CaCl_2$ and 1 mM $MgCl_2$, to which an additional 10 mM $CaCl_2$ was added prior to treatment with 2.5 μM ionomycin (Sigma).

3 Toward practical small molecule T_1 sensors: Improving the longitudinal relaxivity of *Bacillus megaterium* Cytochrome P450 BM3h

3.1 Introduction

Positive contrast agents, those that enhance observable MRI signal, are the optimal mode of contrast for practical application *in vivo* since they locally increase the observed signal-to-noise ratio. As examined in Chapter 1, positive contrast is generally achieved with paramagnetic ions that accelerate the recovery of longitudinal (T_1) relaxation, most often by acting on water molecules coordinated in the so-called inner sphere [27]. Since molecular rearrangements at inorganic ions have long been known to effect their solvent coordination, several groups have shown interest in generating MRI sensors that operate by modulating the number of water coordination sites in the inner sphere. Thus far, such sensors have been chelates of the paramagnetic ions Gd^{3+} or Mn^{2+} [39,40] which are synthetically complex and may have downstream biocompatibility challenges [39]. Moreover, modifications of such synthetic contrast agents to alter their target specificity or optimize other biochemical properties are technically cumbersome.

Alternatively, our group has explored the possibility that metalloproteins found in nature might be engineerable substrates for producing T_1 sensors with mutable specificity [50]. In principle, such protein-based MRI sensors should have tunable biochemical properties, tissue distribution,

pharmacokinetics, and expression patterns that could be optimized through well established molecular biology techniques that have resulted in pioneering protein-based sensors for optical imaging modalities [5,87,90,91,92].

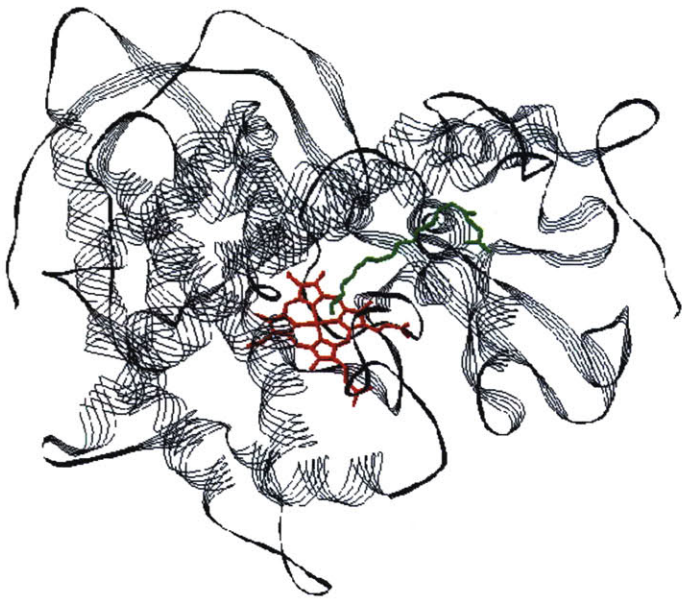

Figure 16. *Bacillus megaterium* cytochrome P-450 BM-3 (CYP102) heme domain (BM3h) ribbon structure with bound N-palmitoyl glycine (green) and heme (iron protoporphyrin IX, red). PDB code 1JPZ.

For generality to future molecules of biological interest, a suitable metalloprotein platform was sought for producing such T_1 sensors. The bacterial hemoprotein cytochrome P450 BM-3 (EC 1.14.14.1) is an NADPH dependent monooxyenase with micromolar affinity for various fatty acid substrates (Figure 16) [93]. In an extensive series of publications, the Arnold group at Caltech has demonstrated that BM-3 can serve as a flexible platform for developing a variety of engineered enzymatic reactions [94,95,96]. Shapiro et al. observed that the heme domain of BM-3 (BM3h) has millimolar affinity for dopamine (DA), a catecholamine neurotransmitter biosynthesized from the amino acid tyrosine. DA is an important intermediary in a vast range of neurological processes including cognition, reward, and learning [97,98]

as well as in disease states such as Parkinson's [99] and schizophrenia [100]. Crystal structures of the wildtype hemoprotein exist in both unbound [101] and fatty acid substrate bound conformations [102]. It is apparent from these structures, as well as other optical characterization, that substrate binding occludes heme-coordinated water, perhaps switching Fe(III) from a hexacoordinate to a pentacoordinate geometry [103].

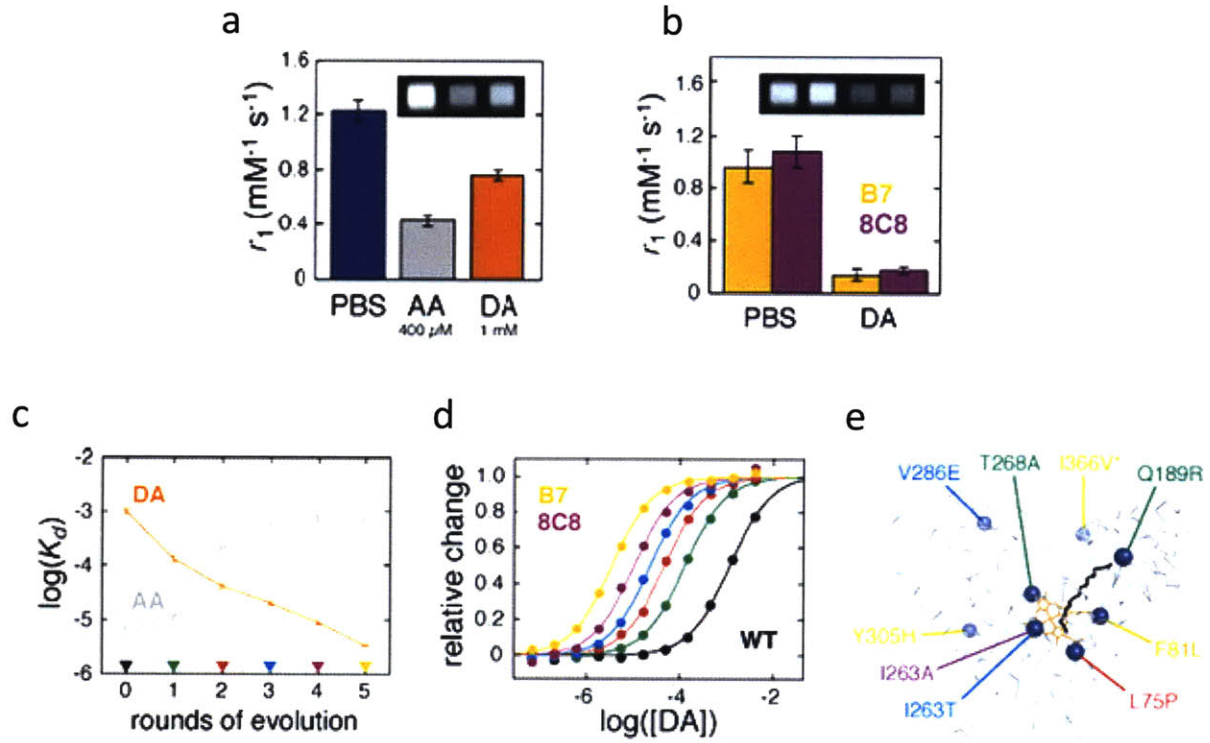

Figure 17. Directed evolution of an MRI contrast sensor for dopamine. (a) Longitudinal relaxivity (r_1) of wild-type cytochrome P-450 BM3h in PBS with or without saturating concentrations of aracadonic acid (AA) or dopamine (DA). (b) Longitudinal relaxivity of evolved DA-binding variants 8C8 and B7 from 4th and 5th round screens, respectively, in the absence or presence of saturating DA (400 μM). (c) Progenitor mutant equilibrium dissociation constants for DA and AA for picked variants in each round of screening. (d) Titration cuves for DA-binding absorbance change for mutants indicated in (c). (e) Mutation map for color-coded mutants in (c) and (d). Adapted from [50].

Since inner sphere T_1 relaxivity is directly proportional to q, the number of water coordination sites, BM3h appeared to be a natural small molecular T_1 sensor. To prove this, the authors examined

BM3h's T_1 relaxation rate when mixed with a natural fatty acid substrate, arachidonic acid (AA), and observed the hypothesized effect (Figure 17a). Then, beginning with the observation that BM3h also binds DA with low affinity, Shapiro et al. performed an iterative screening and selection procedure to generate variants with increased affinity for DA and decreased affinity for the fatty acid arachidonic acid (AA). Over five rounds of evolution, BM3h mutants could be isolated with DA binding affinities in the micromolar range (Figure 17b). Furthermore, the observed T_1 relaxivity of DA-binding BM3h variants could be tuned from around 1 mM^{-1} s^{-1} (4.7 T) in the unbound state to nearly zero in the presence of substrate. Complete abolishment of r_1 implies that DA-bound BM3h variants have $q = 0$ [50].

The utility of this contrast sensor to measure DA in biological context was validated both in tissue culture and *in vivo*. Potassium stimulated DA release from cultured PC12 pheochromocytoma cells resulted in a detectable contrast change for DA-binding variants but not for wildtype BM3h. Furthermore, potassium stimulated DA release could be detected in rat brains by intracranially injected DA-binding variants but not by contralaterally injected wildtype BM3h [50]. In sum, the authors have nicely demonstrated the basic utility of initial versions of engineered T_1 sensors for extracellular DA.

To advance this platform and to aid its practical utility to addressing interesting questions in neuroscience, improvements must be made in the sensor's sensitivity to dynamics in low concentration neurotransmitters. Specifically, detection of low micromolar DA dynamics in reward and learning processes would benefit from a sensor with higher basal T_1 relaxivity, allowing for better sensitivity, shorter scan times, and reducing the minimum concentration required for sensing.

As mentioned in Chapter 1, T_1 relaxation enhancement arises from paramagnetic effects on coordinated and nearby water protons, in a manner modeled by the Solomon, Bloembergen, and Morgan equations (see Section 1.4.1). Among imaginable chemical modifications to the protein that could increase its basal T_1 relaxivity, a relatively straightforward approach would be to increase the total

electron spin, *S*, of its central paramagnetic ion. BM3h's protoporphyrin IX-bound Fe(III) is predominantly low spin (S = 1/2) [104] with a hexacoordinate geometry, an axial cysteine ligand, and a water in the distal coordination site [101]. While Gd(III) would be an excellent choice due to its high spin (*S* = 7/2), Gd(III) is not bioavailable, might exhibit toxicity [105], and could not be accommodated within a porphyrin ring. The next best options would be high spin Fe(III) (S = 5/2), Mn(II) (S = 5/2), or Mn(III) (S = 2). Of these, Mn(III) is the most practical option, since it is generally considered to be obligately high spin and redox stable in biological contexts [106].

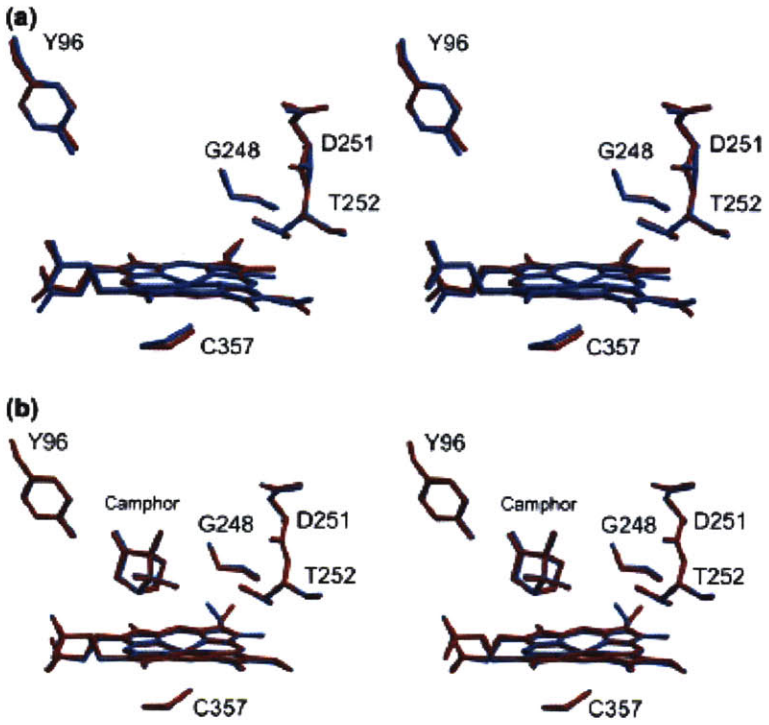

Figure 18. X-ray crystal structure comparison of Mn(III) (red) and Fe(III) (blue) porphyrin containing cytochrome P450cam. (a) Substrate free and (b) camphor substrate bound structures are shown stereoscopically. Adapted from [107].

Since T1 relaxivity is proportional to *S(S+1)* in SBM theory (see Chapter 1.4.1), the relaxivity of low spin BM3h could be increased as much as eight-fold by substituting its prosthetic heme group, Fe(III)

protoporphyrin IX, for Mn(III) protoporphyrin IX (MnPPIX), and assuming that other parameters influencing r_1 are unchanged. Alternatively, relaxivity could be enhanced by as much as 11.7-fold by a mutant in which the native iron heme prosthetic group stably incorporates high spin Fe(III) in a hexacoordinate geometry with a labile water in the distal position. High spin hexacoordinate geometries have been observed in other hemoproteins, including aquomet-myoglobin [108], horse radish peroxidase C bound to benzhydroxamic acid [109], *Streptomyces sp.* catalase-peroxidase [110], as well as others. Crystal structures of the closely related camphor monooxygenase cytochrome P450cam show very minor structural perturbations in the heme binding pocket—distortions that appear to be within the resolution of the crystal structure (Figure 18) [107].

We therefore hypothesized that MnPPIX substituted BM3h variants would exhibit substantially enhanced T_1 relaxivity in exchange for some perturbation of substrate binding affinity. We believe this engineered manganese protein will then serve as a high relaxivity substrate for further directed evolution or rational design of its ligand binding site.

In the remainder of this Chapter, we describe a method to produce high spin MnPPIX-substituted BM3h variants (MnBM3h) and demonstrate that the relaxivity gain is approximately four-fold. I demonstrate that *in vitro* protein refolding has limitingly low efficiency, and we instead propose an "*in vivo*" method to generate MnBM3h during protein expression in *E. coli*. Finally, we will outline initial efforts in collaboration with the Arnold group to produce a high spin Fe(III) variant of BM3h.

3.2 Design

Metalloporphyrin substitution is generally performed by *in vitro* refolding of apoprotein, primarily by batch dilution, dialysis, or chromatographic methods. Success with these methods varies in a protein-specific manner, and screening for refolding conditions is a laborious but critical process to achieve high yields of the desired conformer [111,112].

A method for porphyrin substitution of BM3h has been reported [113]. Recombinant BM3h with modified ferriporphyrins was generated by acetone/HCl precipitation of apoprotein followed by reconstitution with modified porphyrins, ion exchange chromatography, and dialysis. However, thermostability and enzymatic observations arising from control protein refolded with ferric heme suggests that this method does not properly regenerate the original biochemical characteristics of the protein. It is conceivable that the harsh conditions necessary to generate apoprotein in the authors' method might result in protein hydrolysis or sidechain modification. It is also plausible that a distribution of alternate conformations exists in the refolded product. Nonetheless, we examine the method in this work as a starting point for *in vitro* MnPPIX substitution.

Alternatively, bacterial uptake of metalloporphyrins has been demonstrated during recombinant protein expression in *E. coli.* In particular, overexpression of the bacterial transmembrane heme transporter *ChuA* (*ShuA* in *Shigella*) enhances recombinant hemoglobin yield in *E. coli* supplemented with exogenous heme [114]. It has also been shown that *E. coli* overexpressing *ChuA* incorporate exogenous metalloporphyrins into coexpressed protein [115], in a manner that can affect cytochrome function [116]. Similarly, a *HemB*-deficient *E. coli* strain, RP523, demonstrates increased heme uptake through an uncharacterized mechanism (which is likely to be a hypermorphic *ChuA* allele) and can incorporate non-iron metalloporphyrins into coexpressed proteins [117].

Due to its *HemB* deficiency, RP523 requires exogenous heme for growth, resulting in an induction procedure that involves harvesting and resuspension in a heme-free medium for expression of

non-iron metalloporphyrin substituted proteins. Since high throughput (HT) screening of ligand binding variants is a long term aim of this work, it would be optimal to avoid such a media change step in HT format. Accordingly, we opted to clone *ChuA* from O157:H7 enterohemmoragic *E. coli* into a plasmid for inducible coexpression alongside BM3h.

3.3 Results

3.3.1 BM3h apoprotein can be only partially reconstituted with MnPPIX in vitro

Following published methods [113], BM3h apoprotein was precipitated from holoprotein dissolved drip-wise in ice cold acetone/HCl and resolubilized in a buffer containing 8M urea. Partial refolding of apo-BM3h was accomplished by an affinity chromatographic method in which polyhistidine tagged apo-BM3h was immobilized to a Ni-NTA agarose affinity resin under denaturing conditions. Apo-BM3h solutions were reconstituted with MnPPIX while diluting to a urea concentration of ~2M prior to loading on the affinity resin. Protein was then allowed to refold in denaturant-free buffer. Soluble refolded protein could be eluted with native buffer containing imidazole.

Spectrophotometry of desalted eluate showed a unique blue-shifted Soret peak at 373 nm which was distinct from that of free MnPPIX (~367 nm) or of the Soret peak (~420 nm) of native iron-containing BM3h (FeBM3h, Figure 19a). A band with mobility similar to native FeBM3h variants but with distinct unstained coloring was resolvable by separation on a native polyacrylamide gel (Figure 19b). However, refolded MnBM3h samples exhibited a substantial amount of Coomassie Blue-stained

material that appeared in a poorly defined low-mobility smear. Furthermore, circular dichroism (CD) spectra of the samples showed reduced ellipiticity in low wavelengths characteristic of an increase in random coil structure (Figure 20c). Yield of the desired product was estimated to be roughly less than 5%, suggesting that alternate strategies should be explored for producing MnBM3h in large quantities.

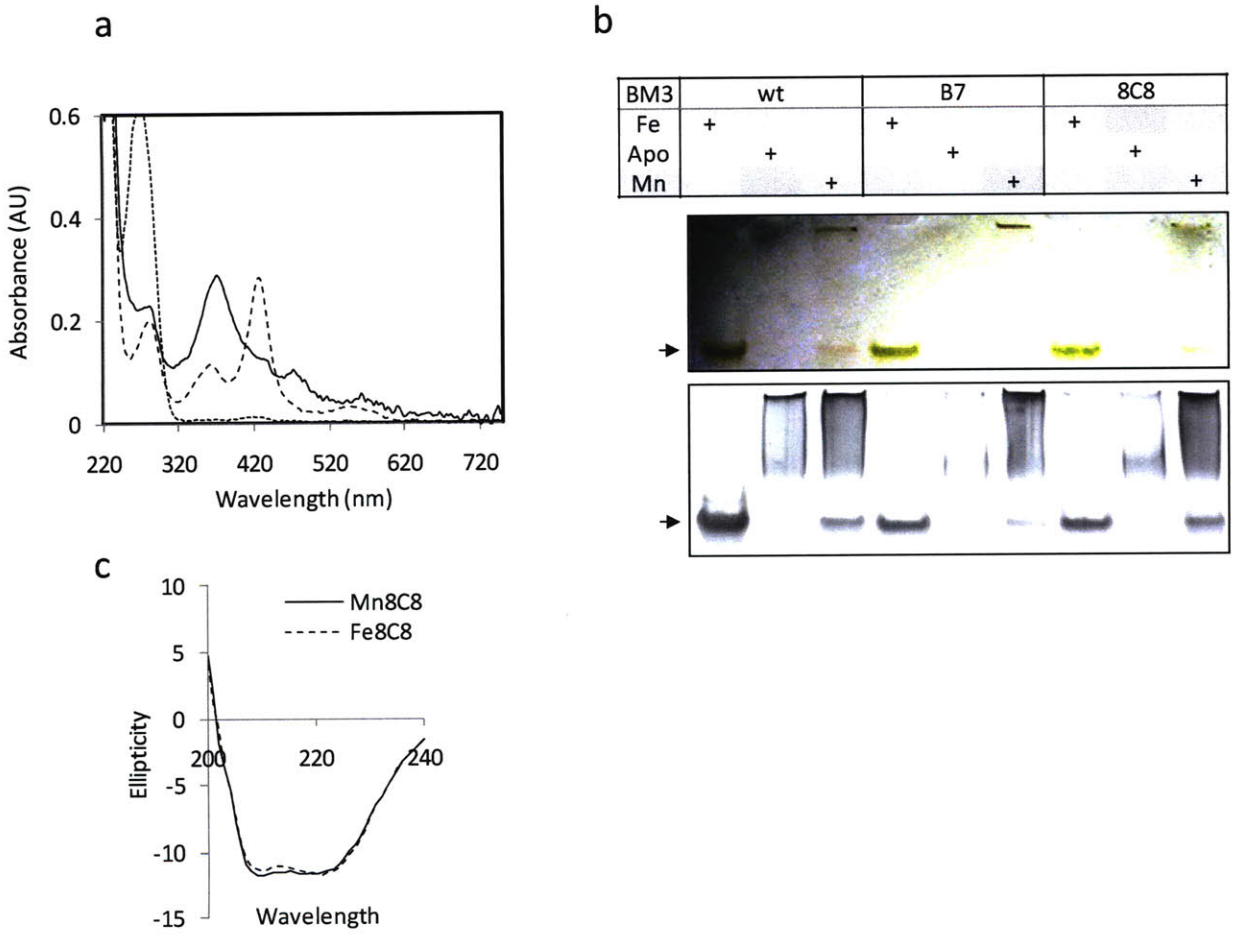

Figure 19. Apoprotein production and low-efficiency refolding of MnBM3h variants using a chromatographic *in vitro* method. (a) UV/Vis absorbance spectra of BM3h-8C8 variant holoprotein (- - -), urea-solubilized apoprotein (----), and MnPPIX substituted sample (—). (b) 7.5% native PAGE separation of holoprotein BM3h variants (FeWT, FeB7, and Fe8C8), apoprotein, and refolded Mn-substituted protein. Top: unstained native protein coloring under white light. Bottom: Coomassie Brilliant Blue G-250 stained. (c) CD spectra of 8C8 holoprotein (- - -) and Mn-substituted protein (—) in 10mM potassium phosphate pH 7.4, 100mM ammonium sulfate.

3.3.2 *BM3h bacterially expressed in iron-free media can be refolded in lysate by addition of MnPPIX*

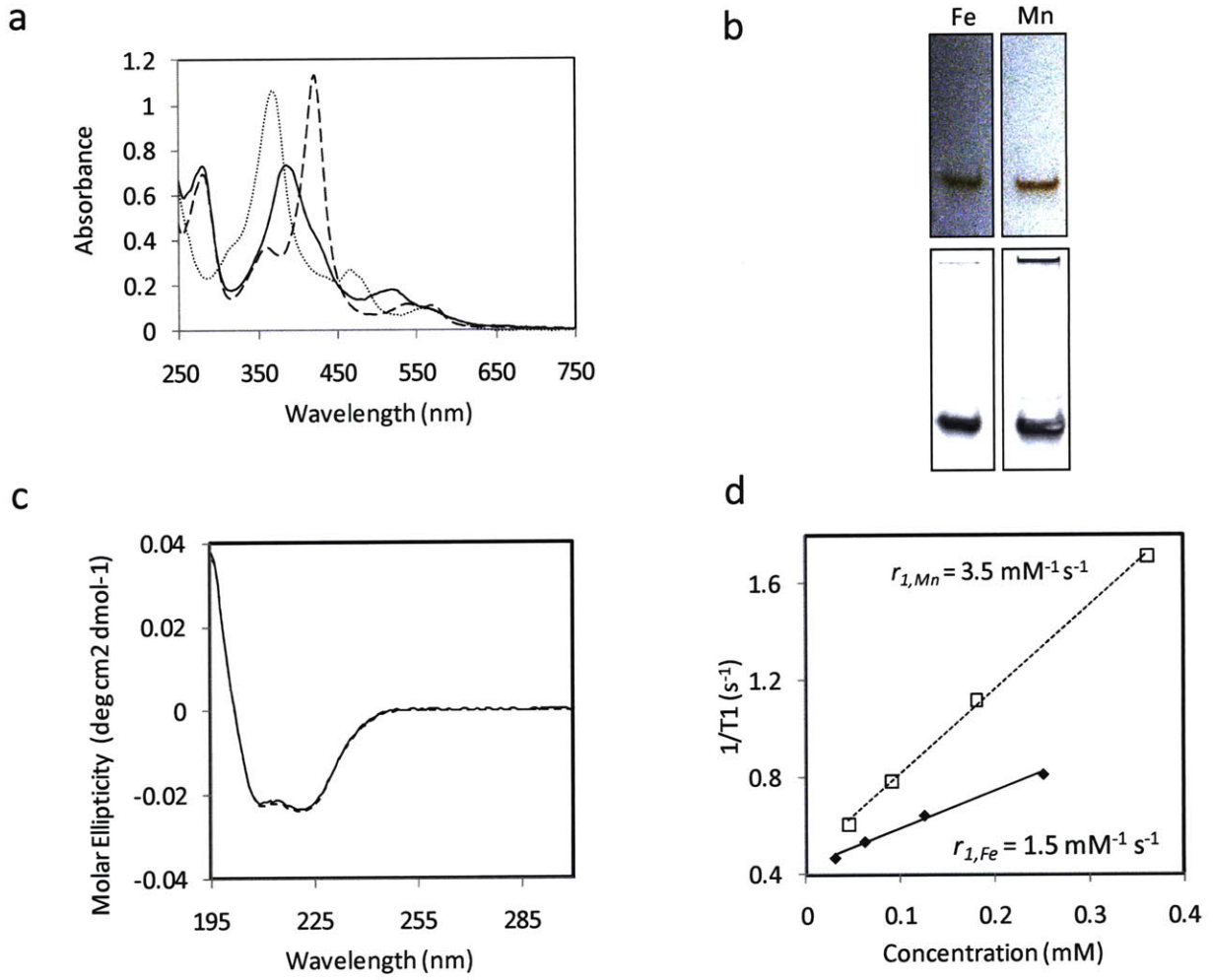

Figure 20. MnBM3h protein from expressed apoprotein in *E. coli* lysates has increased T_1 relaxivity. BL21(DE3) *E. coli* were induced with IPTG to express BM3h in iron-free minimal media, and lysates were incubated overnight with 50 µg/mL MnPPIX prior to purification. (a) UV/Vis absorbance spectra of wt BM3h holoprotein (– –), Mn-substituted protein (—), and free MnPPIX chloride (·····) in PBS. (b) 7.5% native PAGE separation of holoprotein and purified MnBM3h samples. Top: unstained native coloring visualized under white light. Bottom: Coomassie Brilliant Blue G-250 stained. (c) CD spectra of lysate loaded FeBM3h (- - -) and MnBM3h (—) in 10mM potassium phosphate pH 7.4, 100mM ammonium sulfate. (d) T_1 relaxation rates of lysate loaded FeBM3h (•) and MnBM3h (□) in PBS at a range of concentrations. Linear fits give the indicated relaxivities. Concentrations were determined by a colorimetric protein assay, using FeBM3h of known concentration as a standard.

In place of the harsh HCl/acetone procedure to generate apoprotein from holoprotein used above, we sought to express BM3h apoprotein directly in *E. coli* by growth and induction in minimal media lacking iron. Whole lysates generated from these cells were incubated with MnPPIX and subsequently purified under native conditions. The resultant protein exhibited an absorbance peak at 382 nm that was distinct from free MnPPIX and native Fe-BM3h protein (Figure 20a). Native PAGE separation of purified samples revealed a dominant band migrating similarly to Fe-BM3h but with unique unstained coloring. Furthermore, its secondary structure is nearly identical within the resolution of our CD instrument (Figure 20b).

MnBM3h produced by this method showed a >2-fold enhancement in relaxivity (3.5 mM^{-1} s^{-1}) over native FeBM3h (Figure 20c). For this measurement, concentration was determined by standardizing a typical BCA protein assay with native FeBM3h of known concentration (see Methods). It should be noted, however, that the presence of apoprotein in MnBM3h samples would overestimate concentrations—and therefore underestimate relaxivity of the Mn(III)-containing species. It is apparent from the Commassie Blue-stained native gel in Figure 20b that some amount of aggregated protein material is present, most notably visible by blue staining in the sample well. Accordingly, we hypothesize that this relaxivity measurement underestimates the relaxivity of MnBM3h.

3.3.3 Coexpression of O157:H7 ChuA with BM3h variants in MnPPIX-supplemented minimal media results in refolded MnBM3h proteins with improved T1 relaxivity

To improve yield and aide downstream screening procedures, I sought a method to express MnPPIX substituted proteins during expression in *E. coli*. Based on others' work seeking to enhance

bacterial production of recombinant hemoproteins [114,115,117] and to analyze metalloporphyrin effects on respiratory chain function [116], we undertook to coexpress the outer membrane heme receptor *ChuA*. The complete ORF was cloned from O157:H7 genomic DNA into a T7/lacI inducible promoter/repressor expression system. MnBM3h protein could be produced in high yield from BL21(DE3) *E. coli* cotransformed with this *ChuA* construct and an inducible BM3h expression constructs were grown in iron-free minimal media and induced in the presence of supplemented MnPPIX (Figure 21a).

The resultant purified protein shows an absorbance peak at 382 nm, which was similar to that seen for MnBM3h samples refolded in lysate from expressed apoprotein (Figure 21c). Interestingly, the three MnBM3h variants showed differences in the relative amplitude of the absorbance bands at 382 nm and 519 nm compared to that at 280 nm and to the shoulder at 418 nm. Since these variants were evolved for distinct substrate binding specificities, one might postulate that they exhibit differences in their active site conformations and, therefore, in the electronic structure of the MnPPIX coordination field. Nonetheless, the spectra of all three BM3h variants were wholly distinct from that of free MnPPIX and from FeBM3h proteins. The three Mn-substituted variants were also migrated similarly to Fe-containing proteins by native PAGE, showing distinctive unstained color differences between the two metalloporphyrin versions of each variant (Figure 21b).

We next measured the T_1 relaxation rates of purified MnBM3h variants in physiological buffer. Images were taken in a single 1.63mm slice across a 384-well microtiter plate using a multi-spin multi-echo pulse sequence in a 4.7 T MRI scanner (Figure 22). MnBM3h and FeBM3h proteins were diluted at a range of concentrations, and T_1 relaxation rates were fit from scans at a range of repetition times (TR = 73 ms to 5000 ms, TE = 10 ms). FeBM3h concentration was determined spectrophotometrically by CO-binding to reduced BM3h. This FeBM3h protein of known concentration was then used to as a

calibration standard for a bicinchoninic acid (BCA) protein assay to determine the concentrations of MnBM3h protein dilutions.

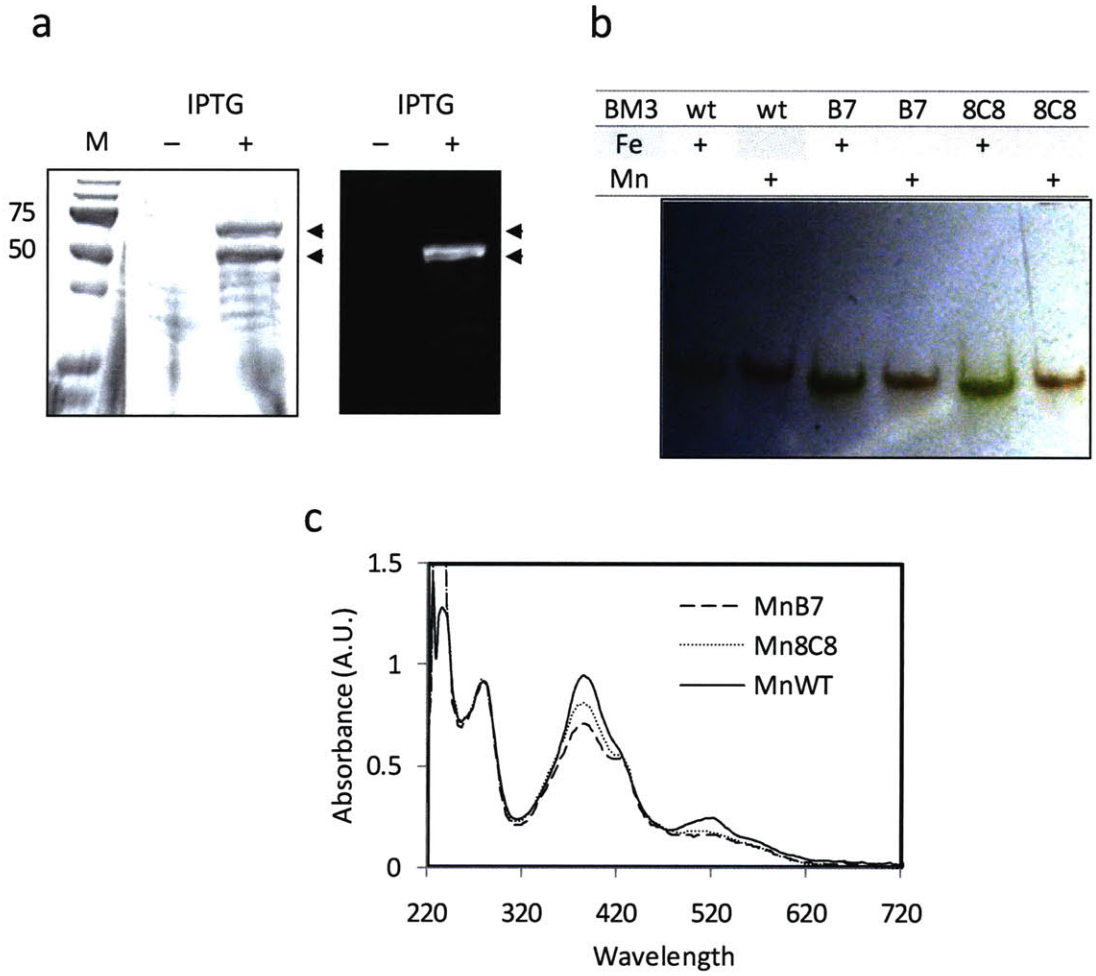

Figure 21. Recombinant expression of MnBM3h proteins in *E. coli* by coexpression of the heme transporter *ChuA*. (a) Coexpression of ChuA and BM3h in IPTG-induced whole bacterial lysates separated by SDS-PAGE. Left: Coomassie Brilliant Blue G-250. Right: Ni-NTA dye stained gel, imaged with UV transillumination. Upper arrow indicates likely ChuA product, and lower arrow indicates His_6-tagged BM3h. (b) Purified FeBM3h and MnBM3h variants from ChuA coexpressing cells separated by 7.5% native PAGE in 50 mM imidazole-HEPES, pH 7.6 and visualized by their native coloring under white light. (c) UV/Vis absorbance spectra of three purified MnBM3h variants in PBS.

Relaxivity is the linear slope relating relaxation rate to contrast agent concentration. The three MnBM3h variants showed, on average, 3.6-fold higher T_1 relaxivity (mean ± S.D. = 5.1 ± 0.6 mM^{-1} s^{-1})

compared to FeBM3h (1.4 mM^{-1} s^{-1}). MnBM3h produced from a wildtype BM3h sequence had the highest relaxivity (5.7 mM^{-1} s^{-1}), whereas mutants MnBM3h-8C8 and MnBM3h-B7 showed relaxivities of 5.0 mM^{-1} s^{-1} and 4.5 mM^{-1} s^{-1}, respectively (Figure 22b). For T_1-weighted scans, this translates directly to a perceptible contrast enhancement at micromolar concentrations in physiological buffer.

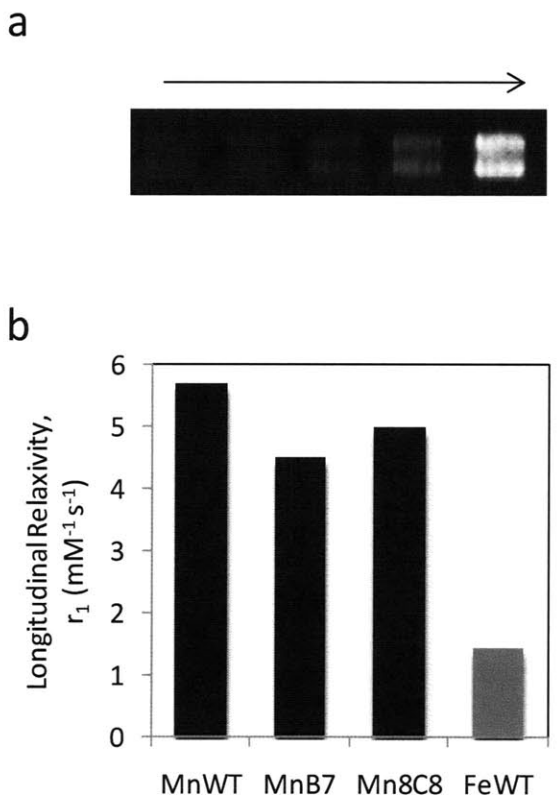

Figure 22. MnBM3h proteins produced in *E. coli* by *ChuA* coexpression show increased T_1 relaxivity. (a) T_1-weighted MSME MRI scan taken in 1.63-mm slice across wells of a 384 well microtiter plate filled with purified MnBM3h-B7 protein in PBS, where concentration increases linearly in the direction of the arrow (TE = 10 ms, TR = 298 ms). (b) T_1 relaxivities fit from data as in (a) taken with TE = 10 ms and TR = 73 ms to 3125 ms at 4.7 T.

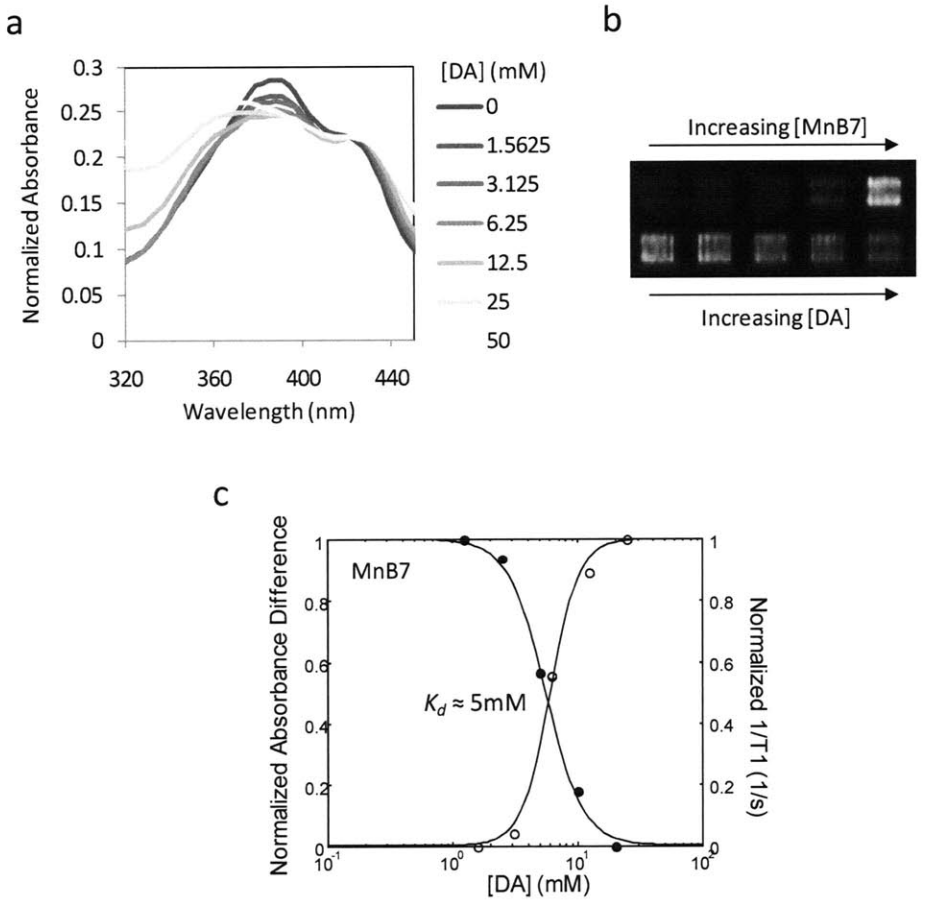

Figure 23. MnB7 binds DA with millimolar affinity and has a DA-dependent T_1 relaxivity effect. (a) UV absorbance spectra of MnB7 protein in PBS mixed with fresh DA at a range of indicated concentrations at room temperature. (b) T_1-weighted MSME MRI scan taken in 1.63-mm slice across wells of a 384 well microtiter plate filled with purified MnBM3h-B7 protein dilutions alone (top row) or with 108 µM protein protein and DA at a range of concentrations (bottom row) in PBS, where concentration of protein (top) or DA (bottom) increases linearly in the direction of the arrow (TE = 10 ms, TR = 298 ms). (b) Normalized T_1 relaxation rates (o) and normalized absorbance difference (•) at a range of DA concentrations. Fit equilibrium dissociation constant $K_d \approx 5$ mM by both methods.

3.3.4 MnBM3h-B7 retains a low dopamine binding affinity and an associated relaxivity effect

Having shown that manganese substitution generates BM3h proteins with improved T_1 relaxivity, we explored whether MnBM3h variants could bind substrates in a manner affecting their

relaxivity. MnPPIX-substituted wildtype BM3h and DA-binding mutants B7 and 8C8 were mixed with dopamine (DA) and were examined by UV/Vis spectrophotometry and T_1-weighted MRI (Figure 23). Difference spectra were taken, and the difference between local minimum and maximum were plotted as a function of ligand concentration [50]. Only MnBM3h-B7 showed measurable affinity for DA at $K_d \approx$ 5 mM. A concomitant effect on T_1 relaxivity was observable, although relaxivity was not entirely abolished even at the highest DA concentrations.

Interestingly, titrations of micromolar concentrations of arachidonic acid (AA) against MnB7 also exhibited a detectable absorbance and relaxivity effect (Figure 24), although the two effects had disagreeing equilibrium dissociation constants ($K_{d,T1}$ = 76 uM, $K_{d,abs}$ = 257 μM), suggesting that they may involve distinct processes or that binding was measured under nonequilibrium conditions.

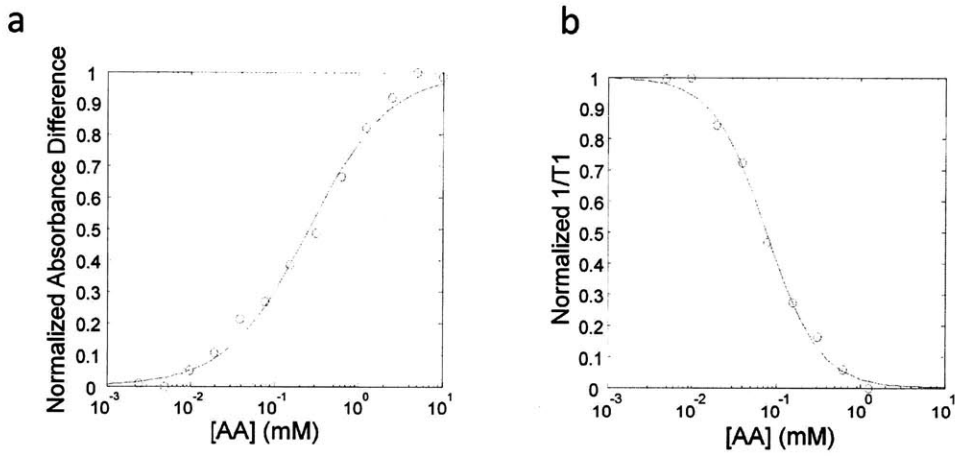

Figure 24. MnBM3h-B7 binds arachidonic acid with micromolar affinity. (a) Normalized absorbance taken from difference spectra of MnBM3h-B7 titrated with AA at a range of concentrations. Fit $K_d \approx$ 76 μM. (b) Normalized change in 1/T1 longitudinal relaxation rates of MnBM3h-B7 titrated with AA at a range of concentrations. Fit $K_d \approx$ 257 μM.

3.4 Discussion and Future Directions

While the observed 3.6-fold mean relaxivity enhancement of manganese substituted BM3h proteins is substantial, it is approximately half of the maximal ideal relaxivity gain expected by SBM theory. As mentioned, the expectation of an 8-fold relaxivity gain is based on a superficial analysis of the differences in total spin of the paramagnetic ions Fe(III), S = ½ in the low spin configuration, and Mn(III), S = 2 in the typical high spin configuration. Importantly, it has been reported that BM3h is in a quantum mixed spin state meaning that the actual spin is between S = 1/2 and S = 5/2 [118]. Shapiro et al. also observed that saturated binding of certain ligands, including dopamine, stabilizes a red-shifted Soret absorbance peak in BM3h proteins, supporting the notion that BM3h is in a mixed spin state [50].

Under the somewhat shaky assumption that spin alone is responsible for the observed differences in relaxivity, then it might be possible to estimate the basal Fe(III) spin based on the fold-change in T1 relaxivity upon manganese substitution (i.e. to a stable S = 2 system). This idealized calculation suggests that $S \approx 0.88$ for Fe(III)-containing BM3h proteins, which one could consider a reasonable number given the small (~3 nm) shift observed upon DA binding [50].

Alternatively, a number of other parameters in SBM inner sphere theory may also change in tandem when switching between the Fe(III) and Mn(III) systems. For example, the bound water residence time, τ_M, and the electron relaxation time, T_{1e}, are likely to be perturbed in somewhat unpredictable ways. Also, subtle changes in the length of the coordinated water-metal bond will strongly affect the distance of closest approach of water protons, which has a dramatic $1/r^6$ impact on inner sphere relaxivity. Accordingly, it is imaginable that a number of these effects are simultaneously at play when comparing the relaxivities of the Mn(III) and Fe(III) containing BM3h proteins. Further

investigations, by NMRD, ESR, and structural methods may help to uncover new avenues of rationally engineerable parameter space to maximize BM3h protein relaxivity. Screening techniques, such as directed evolution, may also be valuable in further maximizing the T1 relaxation properties of the substituted protein.

A negative impact of manganese substitution on ligand binding affinity was expected, but the large magnitude of the effect was somewhat surprising. EPR evidence suggests that Mn(III) may sit somewhat out of the porphyrin plane, perhaps substantially perturbing the cysteine ligand orientation in a manner that occludes substrate binding [119].

That binding of dopamine at high concentrations to the variant MnBM3h-B7 does not completely abolish relaxivity is worthy of further inquiry. There are several noncompeting explanations that could be posited for this effect. First, DA may not bind in a manner that entirely occludes water coordination, such that the observed effects are due to changes in the water exchange rate or outer sphere effects on uncoordinated waters. Less optimistically, it is conceivable that millimolar DA concentrations may have allosteric effects on conformation that could affect water exchange in a manner that does not involve direct DA binding near the metalloporphyrin.

The advancement made here demonstrates a substantially improved static T_1 contrast effect arising from BM3h. Ultimately, we see the value of this work as a platform for developing high relaxivity sensors for molecules of interest in fMRI, such as small molecule neurotransmitters. Advancing to this stage will require yield optimization of the *ChuA* expression system used here to enable high throughput screening approaches in small bacterial culture volumes.

3.5 Materials and Methods

3.5.1 Expression and purification of recombinant BM3h proteins

BM3h proteins were expressed recombinantly in *E. coli* and purified essentially as described [50]. Briefly, terrific broth (TB) containing 100 μg/mL ampicillin or carbenicillin was inoculated 1:100 with a fresh overnight cultures of BL21(DE3) cells (Invitrogen) carrying a pCWori vector containing the open reading frame of wildtype cytochrome P-450 BM-3 generously provided by F Arnold at Caltech. The gene was cloned as a heme domain truncation under the control of a T7/lacI inducible promoter/repressor system, and both wildtype and DA-binding mutants described elsewhere [REF in submission] were used in this study. Cultures were grown with vigorous shaking at 37°C to late log phase ($OD_{600} \approx 0.8 - 1$) and then induced for 18-24 hours at 30°C by addition of 0.6 mM IPTG and supplemented with 0.6 mM δ-aminolevulinic acid (Sigma-Aldrich), a heme precursor. Cells were harvested and lysed using Bugbuster lysis buffer containing lysozyme and benzonase (Novagen) essentially as per the manufacturer's protocol with the addition of an EDTA-free protease inhibitor cocktail set (EMD Biosciences) diluted 1:1000. Lysates were clarified by centrifugation and affinity purified using Ni-NTA agarose Superflow resin (Qiagen) essentially by the manufacturer's protocol. Eluted protein was concentrated in an Amicon Ultra centrifugal filtration device (30 kDa MWCO, Millipore) at 4°C. The filter retentate was then desalted and buffer exchanged by gel filtration on a G-25 sephadex column (GE Amersham) equilibrated with 1X PBS and then reconcentrated. Expression and purity were analyzed by SDS-PAGE with Coomassie Brilliant Blue staining.

3.5.2 *In vitro production of BM3h apoprotein, and affinity chromatographic reconstitution with MnPPIX*

BM3h apoprotein was produced using a method described elsewhere [113]. Briefly, to generate apoprotein, purified BM3h protein at ~200 - 300 μM was added drip-wise to a vigorously stirring bath of ice-cold acetone containing 0.2% (v/v) concentrated HCl. The white precipitate was washed in acetone and dissolved at ~10 mg/mL in 8M urea, 100mM sodium phosphate, 150mM NaCl, pH 8.0 overnight at 4°C.

Aliquots of ~10 mg/mL apoprotein were partially reconstituted by diluting 0.2X into 50mM sodium phosphate pH 8.0, 300mM NaCl, 20mM imidazole, 0.1 mg/mL MnPPIX (from a DMF stock) to a final urea concentration of 1.6M urea. This solution was incubated briefly at room temperature before loading onto a Ni-NTA agarose column. The column was washed extensively with 50mM sodium phosphate pH 8.0, 300mM NaCl, 20mM imidazole buffer and eluted with the same buffer containing 250mM imidazole. The eluate was concentrated using a 30kDa Amicon Ultra centrifugal filter (Millipore) at 4°C. Soluble retentate was then desalted using a PD-10 disposable Sephadex G-25 gel filtration column (GE Amersham) equilibrated in PBS and then reconcentrated by centrifugal filtration. Samples were separated by native PAGE using 4%-7.5% Tris-HCl gels in a 50mM imidazole-HEPES pH 7.5 running buffer at 4°C and proteins were visualized by their native coloring or by Coomassie Brilliant Blue staining (SimplyBlue SafeStain, Invitrogen).

3.5.3 Concentration determination for BM3h and MnBM3h proteins

Purified FeBM3h protein concentration was quantified using a well established carbon monoxide binding assay [50]. Briefly, a series of dilutions of protein were dissolved in of 100mM Tris-HCl pH 8.0, and an aliquot of sodium dithionite was added and rapidly mixed. A blanking UV/Vis spectrum was recorded for the reduced hemoprotein. Protein solutions were then bubbled briefly with CO, and spectra were taken at regular intervals until CO saturation was apparent. Concentration was calculated at 450 nm using a molar extinction coefficient of 91,000 M^{-1} cm^{-1} after a baseline correction with the absorbance at 490 nm. To quantify Mn(III)-substituted BM3h (MnBM3h) concentrations, a colorimetric protein assay (Pierce 660nm Protein Assay, Pierce) was calibrated using dilutions of BM3h protein of predetermined concentration by CO-binding.

3.5.4 Circular dichroism spectrometry

Protein samples were diluted into a 0.2 micron-filtered buffer containing 10mM potassium phosphate pH 7.4, 100mM ammonium sulfate in a quartz cuvette with 1 mm path length. All scans were blanked using the same buffer and cuvette. Ellipticiy was measured between 300nm – 195nm with 2-sec averaging at 25^{o}C in an Aviv Model 202 Circular Dichroism Spectrometer.

3.5.5 *Recombinant production of Mn(III)-substituted BM3h protein by apoprotein refolding in bacterial lysates*

E. coli strain BL21(DE3) transformants carrying pCWori-BM3h plasmid were grown to mid-log phase at 37°C in M9 minimal media supplemented with 2% glucose, 34 μg/mL thiamine, 0.2% casamino acids, 2mM $MgSO_4$ and 0.1mM $CaCl_2$. Cells were then induced overnight at 30°C by addition of 1mM IPTG. Lysates were generated using Bugbuster, benzonase, lysozyme, and protease inhibitors and incubated overnight at 4°C with 50μg/mL MnPPIX from a 5 mg/mL stock in 1:1 DMSO/acetone with 1% (v/v) concentrated HCl. Soluble MnBM3h protein was purified by Ni-NTA agarose affinity chromatography and gel filtration in the same manner as native BM3h proteins. Purity and conformation were assessed by UV/Vis spectrophotometry, SDS-PAGE, native PAGE separation with Coomassie Brilliant Blue staining, and circular dichroism.

3.5.6 *Cloning and expression of the bacterial heme transporter ChuA*

The heme transporter *ChuA* was cloned from O157:H7 *E. coli* genomic DNA (ATCC) using standard directional cloning methods. Briefly, full-length ORF of ChuA was amplified by PCR using primers with 5' extensions containing upstream NcoI and downstream XhoI restriction sites. The amplification product was confirmed by gel electrophoresis, purified, digested with NcoI/XhoI, and ligated into the corresponding sites in a digested pET28a vector (Novagen). Plasmid purified from isolated clones was digested and analyzed by gel electrophoresis and sequenced to confirm the desired construct. For protein expression, single clones were selected on 50 μg/mL kanamycin from chemically

competent BL21(DE3) Star *E. coli* (Invitrogen) transformed with pET28-ChuA. Cultures grown in supplemented M9 minimal media were induced in early-log phase under kanamycin selection, and the IPTG-dependent expression of the desired 72 kDa gene product was confirmed by Coomassie Brilliant Blue staining of SDS-PAGE separated whole cell lysates.

3.5.7 Recombinant production of Mn(III)-substituted BM3h protein by ChuA heme transporter coexpression

Separate plasmids containing *ChuA* and *BM3h* constructs were cotransformed into BL21(DE3) Star *E. coli*, and isolated clones were selected on kanamycin and ampicillin. Vigorously shaking cultures inoculated 1:100 from fresh overnight cultures were grown at 37°C to $OD_{600} \approx 0.4$ in M9 minimal media supplemented with 2% glucose, 34 μg/mL thiamine, 0.2% casamino acids, 2mM $MgSO_4$ and 0.1mM $CaCl_2$. Protein expression was induced overnight at 29°C by addition of 1mM IPTG and the growth medium was simultaneously supplemented with 30 μg/mL MnPPIX from a 3 mg/mL DMSO/acetone/1%(v/v) concentrated HCl stock. Cells were harvested, washed in PBS, and lysed in Bugbuster lysis buffer containing lysozyme, benzonase, and protease inhibitors. Lysates were clarified by centrifugation and incubated overnight at 4°C with Ni-NTA Superflow agarose (Qiagen) and purified under native conditions essentially as described for native BM3h. Purity and conformation were assessed by UV/Vis spectrophotometry, SDS-PAGE, native PAGE separation with Coomassie Brilliant Blue staining, and circular dichroism.

3.5.8 MRI relaxometry

Protein samples were diluted in 0.2 micron filtered phosphate buffered saline (PBS) pH 7.4 into 384-well microtiter plate wells (BD Falcon) in a linear range of concentrations, and peripheral plate wells were filled with buffer alone. The plate was imaged at room temperature in a 4.7 T Bruker Avance animal scanner with a 40cm-bore. Images were taken in a 1.63-mm slice across the plate using a multi-spin multi-echo (MSME) pulse sequence with the following parameters. Time to echo (TE) was 10 ms for all scans. Repetition time (TR) ranged from 73 ms to 5000 ms, and averaging was correspondingly adjusted from 64 to 4 scans per TR. T_1 relaxation rates were fit from reconstructed image data using custom routines developed in Matlab (Mathworks).

3.5.9 Spectrophotometric and relaxometric ligand titration with MnBM3h proteins

Ligand binding titrations were performed essentially as described [50]. Briefly, MnBM3h proteins at ~30μM were mixed in PBS with freshly prepared DA or AA at a range of concentrations in a microtiter plate. Absorbance spectra were taken from 250 nm – 600 nm, and difference spectra were generated by baseline subtraction of protein without ligand. Titrations were plotted as the normalized difference between the local maximum and minimum in the difference spectrum. The data was plotted versus ligand concentration and fit to a sigmoid to determine K_d. Similarly prepared plates were imaged using a MSME pulse sequence, as described above. Titration curves were fitted to normalized T_1 relaxation times as a function of ligand concentration.

4 Conclusions

Advancing neuroscience productively into the "systems" realm relies critically on technology that can assay dynamic molecular phenotype noninvasively as a function of stimuli and genetic manipulations. Noninvasive molecular fMRI would have unique value for interrogating function in the brain, but several obstacles must be overcome to bring such a technique to fruition. In this chapter, I will briefly discuss some of these challenges with reference to the two concrete advances described in this thesis.

First, in designing and building an aggregation device that is calcium-dependent, we demonstrated a new design for derivative devices, employing an engineered multivalent protein crosslinker with molecular specificity to inducibly cluster a contrast agent. Several groups, including our own, have previously conceived of aggregation-based sensors as requiring two chemically-distinct populations of contrast agents that aggregate or disaggregate depending on ligand concentration or enzyme activity [43,45,51]. It is likely that the primary motive for these initial designs was to minimize the interparticle spacing within the aggregate and thereby maximize the corresponding relaxivity gain. However, Monte Carlo simulations of superparamagnetic nanoparticle aggregation recently undertaken in our group have revealed that the critical length scales for interparticle distance are on the order of a few particle diameters [44]. Bennett et al. have also computationally examined the importance of spacing in the context of ferritin aggregates and found the optimal length scale to be far longer, perhaps an order of magnitude larger than the core particle diameter [75]. These computational studies suggest that interparticle spacing may be a more flexible design parameter for aggregation-contrast devices than

previously thought. To our knowledge and as of this writing, computational studies of the effect of interparticle spacing on aggregation-based T_2 relaxation enhancement have not been fully validated by empirical results. This is undoubtedly a potential avenue of future work, as improvements in the theoretical underpinnings of aggregation-based contrast mechanisms can be employed to design optimal sensors for molecular fMRI.

Any engineered contrast agent for molecular imaging must be deliverable *in vivo*. Especially for those sensors whose intended function is intracellular, our long term approach will be to exploit well established genetic strategies for tissue specific expression *in vivo* [35]. However, the *in vivo* context brings with it enormous peripheral complexity and day-to-day technical uncertainty, which may yield limited instructive value from the immediate application of these nascent technologies in live animals. Much can be learned about optimizing design and experimental strategies in cell culture, as has been the case in other imaging modalities.

Of specific concern are endogenous factors that could readily compete for interactions with sensor components, especially those that are based on modified normal cellular proteins, such as those employed in the calcium sensor presented here. It is conceivable that these off-target effects will mean that higher (and therefore less efficient) concentrations of sensing components will be necessary for operation above these "nonspecific" interactions. This criterion must then be balanced against the impact of high sensor concentrations on normal cell processes. Nagai et al. have demonstrated that genetically-encoded fluorescence sensors can provide meaningful insights into calcium dynamics despite the potential for off-target interactions [47], but efforts to eschew these interactions have also been undertaken [87]. These efforts, as well as our own [88], should undoubtedly be exploited in future refinements of our MRI calcium sensor. For example, a skeptical analysis of *in vitro* pilot tests (described in Section 2.4.5) of calcium-dependent sensor aggregation in dilute cell lysate lends credence to this

concern, since less overall aggregation was found to occur for any given incubation ratio than in buffer alone (Figure 13). Future work to produce orthogonal binding partners selected away from significant off-target interactions would yield a device that interacts minimally with confounding cellular components.

Aggregation based T_2 sensors have the potential to be sensitive to vanishingly small concentration dynamics, where their primary limitation will be in the kinetics of aggregation and disaggregation. On the other hand, T_1 sensors, as we have thus far conceived of them, must tackle certain pragmatic problems related to their low basal relaxivities and the low endogenous concentrations of interesting targets. Without significant technological advancement, it will be challenging to detect nanomolar dynamics using contrast sensor concentrations in the tens of micromolar above instrument noise.

In this work, we have begun to address that concern by producing an engineered metalloprotein consisting of manganese porphyrin substituted cytochrome P-450 BM3h. The signal gain associated with this advancement was approximately 3.6-fold at 4.7 T, which translates directly into an equivalent MRI signal gain for any given concentration employed *in vivo*. Accordingly, contrast could be achieved in the low micromolar range using this new agent, and a 1% change in sensor relaxivity could then be detectable for ligands in the hundreds-of-nanomolar range on our instrument. This is a significant advancement and brings the dynamics of numerous neurological targets within sensible reach, including an array of synaptic neurotransmitters and intracellular second messengers.

As a platform for T_1 sensors for molecular fMRI, the future challenge for MnBM3h will be to develop binding affinity for interesting molecular targets. In this regard, fruitful efforts by Frances Arnold in collaboration with our group to use directed evolution as a means to select for desirable traits in cytochrome P450 enzymes have already yielded BM3h variants with high affinity for dopamine [50].

Work is already underway to adapt the *ChuA*-mediated porphyrin substitution expression system described here and pioneered by others [114,115,117] to a high throughput screening format. Such developments will permit further screening-based optimization of important parameters for future applications, including binding affinity, kinetics and thermostability.

Technological advancement of practical molecular fMRI sensors is a unique biological engineering challenge, one that draws interdisciplinary knowledge from a range of fields and techniques. As observed in other applications, protein engineering approaches that take advantage of both rational design and evolutionary refinement exhibit the most demonstrative success. Since the design efforts described here have been rational in nature, further advancement should undoubtedly exploit the tremendous possibilities of directed evolution. The observable results of natural evolution—the vast molecular complexity of nature—should give confidence that simple genetically-encodable devices are within the biological engineer's grasp.

5 References

[1] S. Ogawa, T. Lee, A. Kay, D. Tank, Brain magnetic resonance imaging with contrast dependent on blood oxygenation, Proceedings Of The National Academy Of Sciences. (1990).

[2] A. Jasanoff, Bloodless fMRI, 2007.

[3] D.J. Heeger, D. Ress, What does fMRI tell us about neuronal activity?, Nature Reviews. Neuroscience. 3 (2002) 142-51.

[4] A. Jasanoff, Functional MRI using molecular imaging agents, 2005.

[5] R. Tsien, A. Miyawaki, Fluorescent protein sensors for detection of analytes, US Patent App. 11/334,622. (2006).

[6] B. Giepmans, S. Adams, M. Ellisman, R. Tsien, The fluorescent toolbox for assessing protein location and function, Science. (2006).

[7] M. Phelps, PET: molecular imaging and its biological applications, (2004).

[8] N. Logothetis, What we can do and what we cannot do with fMRI, Nature. (2008).

[9] F. Patolsky, B.P. Timko, G. Yu, Y. Fang, A.B. Greytak, G. Zheng, et al., Detection, stimulation, and inhibition of neuronal signals with high-density nanowire transistor arrays., Science (New York, N.Y.). 313 (2006) 1100-4.

[10] M.W. Kirschner, The meaning of systems biology., Cell. 121 (2005) 503-4.

[11] L. Luo, E. Callaway, K. Svoboda, Genetic dissection of neural circuits, Neuron. (2008).

[12] I.R. Wickersham, D.C. Lyon, R.J. Barnard, T. Mori, S. Finke, K. Conzelmann, et al., Monosynaptic restriction of transsynaptic tracing from single, genetically targeted neurons., Neuron. 53 (2007) 639-47.

[13] R. Weissleder, U. Mahmood, Molecular imaging., Radiology. 219 (2001) 316-33.

[14] A. Jasanoff, MRI contrast agents for functional molecular imaging of brain activity, Current Opinion In Neurobiology. (2007).

[15] R. Weissleder, V. Ntziachristos, Shedding light onto live molecular targets, Nature Medicine. (2003).

[16] L. Pauling, C.D. Coryell, The Magnetic Properties and Structure of Hemoglobin, Oxyhemoglobin and Carbonmonoxyhemoglobin., Proceedings Of The National Academy Of Sciences Of The United States Of America. 22 (1936) 210-6.

[17] C.T. Kapff, J.H. Jandl, Blood, atlas and sourcebook of hematology, n.d.

[18] D.J. Heeger, A.C. Huk, W.S. Geisler, D.G. Albrecht, Spikes versus BOLD: what does neuroimaging tell us about neuronal activity?, Nature Neuroscience. 3 (2000) 631-3.

[19] N.K. Logothetis, J. Pauls, M. Augath, T. Trinath, A. Oeltermann, Neurophysiological investigation of the basis of the fMRI signal., Nature. 412 (2001) 150-7.

[20] A. Devor, Coupling of Total Hemoglobin Concentration, Oxygenation, and Neural Activity in Rat Somatosensory Cortex, Neuron. 39 (2003) 353-359.

[21] R. Birn, Z. Saad, P. Bandettini, Spatial heterogeneity of the nonlinear dynamics in the FMRI BOLD response, Neuroimage. (2001).

[22] S.A. Sheth, M. Nemoto, M. Guiou, M. Walker, N. Pouratian, A.W. Toga, Linear and Nonlinear Relationships between Neuronal Activity, Oxygen Metabolism, and Hemodynamic Responses, Neuron. 42 (2004) 347-355.

[23] C. Westbrook, C. Kaut-Roth, J. Talbot, MRI in practice, n.d.

[24] N. Bloembergen, Relaxation Effects in Nuclear Magnetic Resonance Absorption, Physical Review. 73 (n.d.).

[25] A. Nolle, L. Morgan, Frequency dependence of proton spin relaxation in aqueous solutions of paramagnetic ions, The Journal Of Chemical Physics. (1957).

[26] I. Solomon, Relaxation Processes in a System of Two Spins, Physical Review. 99 (n.d.).

[27] R.E. Lauffer, Paramagnetic Metal Complexes as Water Proton Relaxation Agents for NMR Imaging: Theory and Design, Chemical Reviews. (1987).

[28] A. Roch, R. Muller, P. Gillis, Theory of proton relaxation induced by superparamagnetic particles, The Journal Of Chemical Physics. (1999).

[29] R. Muller, P. Gillis, F. Moiny, A. Roch, Transverse relaxivity of particulate MRI contrast media: from theories to experiments, Magnetic Resonance In Medicine. (1991).

[30] J. Freed, Dynamic effects of pair correlation functions on spin relaxation by translational diffusion in ..., The Journal Of Chemical Physics. (1978).

[31] L. Hwang, J. Freed, Dynamic effects of pair correlation functions on spin relaxation by translational diffusion in ..., The Journal Of Chemical Physics. (1975).

[32] I. Bertini, J. Kowalewski, C. Luchinat, T. Nilsson, G. Parigi, Nuclear spin relaxation in paramagnetic complexes of S=1: Electron spin relaxation effects, The Journal Of Chemical Physics. 111 (1999) 5795.

[33] Y. Gossuin, P. Gillis, A. Hocq, Q.L. Vuong, A. Roch, Magnetic resonance relaxation properties of superparamagnetic particles, Wiley Interdisciplinary Reviews: Nanomedicine And Nanobiotechnology. 1 (2009) 299-310.

[34] A. Roch, Y. Gossuin, R. Muller, P. Gillis, Superparamagnetic colloid suspensions: water magnetic relaxation and clustering, Journal Of Magnetism And Magnetic Materials. (2005).

[35] G. Westmeyer, A. Jasanoff, Genetically controlled MRI contrast mechanisms and their prospects in systems neuroscience research, Magnetic Resonance Imaging. (2007).

[36] Y.J. Lin, A.P. Koretsky, Manganese ion enhances T1-weighted MRI during brain activation: an approach to direct imaging of brain function., Magnetic Resonance In Medicine : Official Journal Of The Society Of Magnetic Resonance In Medicine / Society Of Magnetic Resonance In Medicine. 38 (1997) 378-88.

[37] R.G. Pautler, A.P. Koretsky, Tracing odor-induced activation in the olfactory bulbs of mice using manganese-enhanced magnetic resonance imaging., NeuroImage. 16 (2002) 441-8.

[38] M. Shapiro, T. Atanasijevic, H. Faas, G. Westmeyer, A. Jasanoff, Dynamic imaging with MRI contrast agents: quantitative considerations, Magnetic Resonance Imaging. (2006).

[39] A.C. Esqueda, J.A. López, G. Andreu-de-Riquer, J.C. Alvarado-Monzón, J. Ratnakar, A.J. Lubag, et al., A New Gadolinium-Based MRI Zinc Sensor., Journal Of The American Chemical Society. (2009).

[40] X. Zhang, K.S. Lovejoy, A. Jasanoff, S.J. Lippard, Water-soluble porphyrins as a dual-function molecular imaging platform for MRI and fluorescence zinc sensing., Proceedings Of The National Academy Of Sciences Of The United States Of America. 104 (2007) 10780-5.

[41] W. Li, S. Fraser, T. Meade, A calcium-sensitive magnetic resonance imaging contrast agent, J. Am. Chem. Soc. (1999).

[42] H.B. Na, I.C. Song, T. Hyeon, Inorganic Nanoparticles for MRI Contrast Agents, Advanced Materials. 21 (2009) 2133-2148.

[43] J.M. Perez, L. Josephson, T. O'Loughlin, D. Högemann, R. Weissleder, Magnetic relaxation switches capable of sensing molecular interactions., Nature Biotechnology. 20 (2002) 816-20.

[44] Y. Matsumoto, A. Jasanoff, T2 relaxation induced by clusters of superparamagnetic nanoparticles: Monte Carlo simulations., Magnetic Resonance Imaging. 26 (2008) 994-8.

[45] T. Atanasijevic, M. Shusteff, P. Fam, A. Jasanoff, Calcium-sensitive MRI contrast agents based on superparamagnetic iron oxide nanoparticles and ..., PNAS. (2006).

[46] E.M. Callaway, A molecular and genetic arsenal for systems neuroscience., Trends In Neurosciences. 28 (2005) 196-201.

[47] T. Nagai, A. Sawano, E.S. Park, A. Miyawaki, Circularly permuted green fluorescent proteins engineered to sense Ca2+., Proceedings Of The National Academy Of Sciences Of The United States Of America. 98 (2001) 3197-202.

[48] B. Rao, D. Lauffenburger, K. Wittrup, Integrating cell-level kinetic modeling into the design of engineered protein therapeutics, Nature Biotechnology. (2005).

[49] J. Bloom, F. Arnold, In the light of directed evolution: Pathways of adaptive protein evolution, Proceedings Of The National Academy Of Sciences. (2009).

[50] M.G. Shapiro, G.G. Westmeyer, P. Romero, J.O. Szablowski, B. Küster, A. Shah, et al., Directed evolution of an MRI contrast agent for noninvasive imaging of dopamine (Submitted), (n.d.).

[51] M. Shapiro, J. Szablowski, R. Langer, A. Jasanoff, Protein Nanoparticles Engineered to Sense Kinase Activity in MRI, Journal Of The American Chemical Society. (2009).

[52] B. Cohen, H. Dafni, G. Meir, A. Harmelin, Ferritin as an endogenous MRI reporter for noninvasive imaging of gene expression in C6 ..., Neoplasia. (2005).

[53] B. Cohen, K. Ziv, V. Plaks, T. Israely, MRI detection of transcriptional regulation of gene expression in transgenic mice, Weizmann.ac.il. (2007).

[54] E.T. Ahrens, U. Rothbächer, R.E. Jacobs, S.E. Fraser, A model for MRI contrast enhancement using T1 agents, Proceedings Of The National Academy Of Sciences Of The United States Of America. 95 (1998).

[55] X. Liu, E. Theil, Ferritins: dynamic management of biological iron and oxygen chemistry, Acc. Chem. Res. (2005).

[56] Y. Gossuin, R.N. Muller, P. Gillis, Relaxation induced by ferritin: a better understanding for an improved MRI iron quantification., NMR In Biomedicine. 17 (2004) 427-32.

[57] Y. Gossuin, P. Gillis, R.N. Muller, A. Hocq, Relaxation by clustered ferritin: a model for ferritin-induced relaxation in vivo., NMR In Biomedicine. 20 (2007) 749-56.

[58] J.T. Littleton, M. Stern, M. Perin, H.J. Bellen, Calcium dependence of neurotransmitter release and rate of spontaneous vesicle fusions are altered in Drosophila synaptotagmin mutants., Proceedings Of The National Academy Of Sciences Of The United States Of America. 91 (1994) 10888-92.

[59] A. Ghosh, M.E. Greenberg, Calcium signaling in neurons: molecular mechanisms and cellular consequences, Science. 268 (1995) 239-247.

[60] R. Nicoll, The coupling of neurotransmitter receptors to ion channels in the brain, Science. (1988).

[61] M. Sheng, M. Kim, Postsynaptic signaling and plasticity mechanisms, Science. (2002).

[62] G. Gasic, M. Hollmann, Molecular neurobiology of glutamate receptors, Annual Review Of Physiology. (1992).

[63] T. Collin, A. Marty, I. Llano, Presynaptic calcium stores and synaptic transmission., Current Opinion In Neurobiology. 15 (2005) 275-81.

[64] N.J. Emptage, C.A. Reid, A. Fine, Calcium stores in hippocampal synaptic boutons mediate short-term plasticity, store-operated Ca2+ entry, and spontaneous transmitter release., Neuron. 29 (2001) 197-208.

[65] F. Helmchen, K. Imoto, B. Sakmann, Ca2+ buffering and action potential-evoked Ca2+ signaling in dendrites of pyramidal neurons., Biophysical Journal. 70 (1996) 1069-81.

[66] G. Grynkiewicz, M. Poenie, R. Tsien, A new generation of Ca2+ indicators with greatly improved fluorescence properties, Journal Of Biological Chemistry. (1985).

[67] J. Nakai, M. Ohkura, K. Imoto, A high signal-to-noise Ca2+ probe composed of a single green fluorescent protein, Nature Biotechnology. (2001).

[68] Y.N. Tallini, M. Ohkura, B. Choi, G. Ji, K. Imoto, R. Doran, et al., Imaging cellular signals in the heart in vivo: Cardiac expression of the high-signal Ca2+ indicator GCaMP2., Proceedings Of The National Academy Of Sciences Of The United States Of America. 103 (2006) 4753-8.

[69] J.M. Perez, L. Josephson, R. Weissleder, Use of magnetic nanoparticles as nanosensors to probe for molecular interactions., Chembiochem : A European Journal Of Chemical Biology. 5 (2004) 261-4.

[70] O. Griesbeck, G.S. Baird, R.E. Campbell, D.A. Zacharias, R.Y. Tsien, Reducing the environmental sensitivity of yellow fluorescent protein. Mechanism and applications., The Journal Of Biological Chemistry. 276 (2001) 29188-94.

[71] G. Cairo, E. Rappocciolo, L. Tacchini, L. Schiaffonati, Expression of the genes for the ferritin H and L subunits in rat liver and heart. Evidence for tissue-specific regulations at pre- and post-translational levels., The Biochemical Journal. 275 (Pt 3 (1991) 813-6.

[72] N.D. Chasteen, P.M. Harrison, Mineralization in ferritin: an efficient means of iron storage., Journal Of Structural Biology. 126 (1999) 182-94.

[73] Y. Gossuin, A. Roch, R.N. Muller, P. Gillis, Relaxation Induced by Ferritin and Ferritin-Like Magnetic Particles: The Role of Proton Exchange, Magnetic Resonance In Medicine. 243 (2000) 237-243.

[74] G. Genove, U. DeMarco, H. Xu, W. Goins, A new transgene reporter for in vivo magnetic resonance imaging, Nature Medicine. (2005).

[75] K.M. Bennett, E.M. Shapiro, C.H. Sotak, A.P. Koretsky, Controlled aggregation of ferritin to modulate MRI relaxivity., Biophysical Journal. 95 (2008) 342-51.

[76] G.S. Baird, D.A. Zacharias, R.Y. Tsien, Biochemistry, mutagenesis, and oligomerization of DsRed, a red fluorescent protein from coral., Proceedings Of The National Academy Of Sciences Of The United States Of America. 97 (2000) 11984-9.

[77] B. Bevis, B. Glick, Rapidly maturing variants of the Discosoma red fluorescent protein (DsRed), Nature Biotechnology. (2002).

[78] D.E. Strongin, B. Bevis, N. Khuong, M.E. Downing, R.L. Strack, K. Sundaram, et al., Structural rearrangements near the chromophore influence the maturation speed and brightness of DsRed variants., Protein Engineering, Design & Selection : PEDS. 20 (2007) 525-34.

[79] X. Wang, R. Qiu, W. Tsark, Q. Lu, Rapid promoter analysis in developing mouse brain and genetic labeling of young neurons by doublecortin-DsRed-express., Journal Of Neuroscience Research. 85 (2007) 3567-73.

[80] S. Levi, A. Luzzago, G. Cesareni, A. Cozzi, F. Franceschinelli, A. Albertini, et al., Mechanism of ferritin iron uptake: activity of the H-chain and deletion mapping of the ferro-oxidase site. A study of iron uptake and ferro-oxidase activity of human liver, recombinant H-chain ferritins, and of two H-chain deletion mutants., The Journal Of Biological Chemistry. 263 (1988) 18086-92.

[81] P. Santambrogio, S. Levi, A. Cozzi, E. Rovida, A. Albertini, P. Arosio, Production and characterization of recombinant heteropolymers of human ferritin H and L chains., The Journal Of Biological Chemistry. 268 (1993) 12744-8.

[82] T.J. Lukas, W.H. Burgess, F.G. Prendergast, W. Lau, D.M. Watterson, Calmodulin binding domains: characterization of a phosphorylation and calmodulin binding site from myosin light chain kinase., Biochemistry. 25 (1986) 1458-64.

[83] B.F. Pfleger, N.J. Fawzi, J.D. Keasling, Optimization of DsRed production in Escherichia coli: effect of ribosome binding site sequestration on translation efficiency., Biotechnology And Bioengineering. 92 (2005) 553-8.

[84] J.J. Mayo, P. Kohlhepp, D. Zhang, J.J. Winzerling, Effects of sham air and cigarette smoke on A549 lung cells: implications for iron-mediated oxidative damage., American Journal Of Physiology. Lung Cellular And Molecular Physiology. 286 (2004) L866-76.

[85] C. Liu, T. Hermann, Characterization of ionomycin as a calcium ionophore, Journal Of Biological Chemistry. (1978).

[86] A. Miyawaki, O. Griesbeck, R. Heim, R.Y. Tsien, Dynamic and quantitative Ca2+ measurements using improved cameleons., Proceedings Of The National Academy Of Sciences Of The United States Of America. 96 (1999) 2135-40.

[87] A.E. Palmer, M. Giacomello, T. Kortemme, S.A. Hires, V. Lev-Ram, D. Baker, et al., Ca2+ indicators based on computationally redesigned calmodulin-peptide pairs., Chemistry & Biology. 13 (2006) 521-30.

[88] D.F. Green, A.T. Dennis, P.S. Fam, B. Tidor, A. Jasanoff, Rational design of new binding specificity by simultaneous mutagenesis of calmodulin and a target peptide., Biochemistry. 45 (2006) 12547-59.

[89] F. Kadir, F. AL-MASSAD, G. Moore, Haem binding to horse spleen ferritin and its effect on the rate of iron release, Biochem. J. (1992).

[90] T. Nagai, A. Sawano, E. Park, A. Miyawaki, Circularly permuted green fluorescent proteins engineered to sense Ca2+, Proceedings Of The National Academy Of Sciences. (2001).

[91] V.O. Nikolaev, M. Bünemann, L. Hein, A. Hannawacker, M.J. Lohse, Novel single chain cAMP sensors for receptor-induced signal propagation., The Journal Of Biological Chemistry. 279 (2004) 37215-8.

[92] S. Okumoto, L.L. Looger, K.D. Micheva, R.J. Reimer, S.J. Smith, W.B. Frommer, Detection of glutamate release from neurons by genetically encoded surface-displayed FRET nanosensors., Proceedings Of The National Academy Of Sciences Of The United States Of America. 102 (2005) 8740-5.

[93] R.T. Ruettinger, L.P. Wen, A.J. Fulco, Coding nucleotide, 5' regulatory, and deduced amino acid sequences of P-450BM-3, a single peptide cytochrome P-450:NADPH-P-450 reductase from Bacillus megaterium., The Journal Of Biological Chemistry. 264 (1989) 10987-95.

[94] A. Glieder, E. Farinas, F. Arnold, Laboratory evolution of a soluble, self-sufficient, highly active alkane hydroxylase, Nature Biotechnology. (2002).

[95] P. Cirino, F. Arnold, Protein engineering of oxygenases for biocatalysis, Current Opinion In Chemical Biology. (2002).

[96] M. Peters, P. Meinhold, A. Glieder, F. Arnold, Regio-and enantioselective alkane hydroxylation with engineered cytochromes P450 BM-3, J. Am. Chem. Soc. (2003).

[97] S. Hyman, R. Malenka, E. Nestler, Neural mechanisms of addiction: the role of reward-related learning and memory, (2006).

[98] W. Schultz, Multiple dopamine functions at different time courses, (2007).

[99] P. Damier, E.C. Hirsch, Y. Agid, A.M. Graybiel, The substantia nigra of the human brain. II. Patterns of loss of dopamine-containing neurons in Parkinson's disease., Brain : A Journal Of Neurology. 122 (Pt 8 (1999) 1437-48.

[100] K. Davis, R. Kahn, G. Ko, M. Davidson, Dopamine in schizophrenia: a review and reconceptualization, American Journal Of Psychiatry. (1991).

[101] K.G. Ravichandran, S.S. Boddupalli, C.A. Hasermann, J.A. Peterson, J. Deisenhofer, Crystal structure of hemoprotein domain of P450BM-3, a prototype for microsomal P450's., Science (New York, N.Y.). 261 (1993) 731-6.

[102] D.C. Haines, D.R. Tomchick, M. Machius, J.A. Peterson, Pivotal role of water in the mechanism of P450BM-3., Biochemistry. 40 (2001) 13456-65.

[103] S.N. Daff, S.K. Chapman, K.L. Turner, R.A. Holt, S. Govindaraj, T.L. Poulos, et al., Redox control of the catalytic cycle of flavocytochrome P-450 BM3., Biochemistry. 36 (1997) 13816-23.

[104] J.S. Miles, A.W. Munro, B.N. Rospendowski, W.E. Smith, J. McKnight, A.J. Thomson, Domains of the catalytically self-sufficient cytochrome P-450 BM-3. Genetic construction, overexpression, purification and spectroscopic characterization., The Biochemical Journal. 288 (Pt 2 (1992) 503-9.

[105] W. Cacheris, S. Quay, S. Rocklage, The relationship between thermodynamics and the toxicity of gadolinium complexes., Magnetic Resonance Imaging. (1990).

[106] J. Krzystek, J. Telser, L.A. Pardi, D.P. Goldberg, B.M. Hoffman, L. Brunel, High-Frequency and - Field Electron Paramagnetic Resonance of High-Spin Manganese(III) in Porphyrinic Complexes., Inorganic Chemistry. 38 (1999) 6121-6129.

[107] T. Makris, K. Koenig, I. Schlichting, S. Sligar, The status of high-valent metal oxo complexes in the P450 cytochromes, Journal Of Inorganic Biochemistry. (2006).

[108] J. Lin, L.B. Vitello, J.E. Erman, Imidazole binding to horse metmyoglobin: dependence upon pH and ionic strength., Archives Of Biochemistry And Biophysics. 352 (1998) 214-28.

[109] G. Smulevich, A. Feis, C. Indiani, M. Becucci, M.P. Marzocchi, Peroxidase-benzhydroxamic acid complexes: spectroscopic evidence that a Fe-H 2 O distance of 2.6 Å can correspond to hexa-coordinate high-spin heme, Journal Of Biological Inorganic Chemistry. 4 (1999) 39-47.

[110] H. Youn, Y. Yim, K. Kim, Y.C. Hah, S. Kang, Spectral Characterization and Chemical Modification of Catalase-Peroxidase from Streptomyces sp., Journal Of Biological Chemistry. 270 (1995) 13740-13747.

[111] E.D. Clark, Refolding of recombinant proteins, Current Opinion In Biotechnology. (1998).

[112] M. Li, Z. Su, J. Janson, In vitro protein refolding by chromatographic procedures, Protein Expression And Purification. (2004).

[113] S. Modi, W. Primrose, L. Lian, G. Roberts, Effect of replacement of ferriprotoporphyrin IX in the haem domain of cytochrome P-450 BM-3 ..., Biochem. J. (1995).

[114] D.M. Villarreal, C.L. Phillips, A.M. Kelley, S. Villarreal, A. Villaloboz, P. Hernandez, et al., Enhancement of recombinant hemoglobin production in Escherichia coli BL21(DE3) containing the Plesiomonas shigelloides heme transport system., Applied And Environmental Microbiology. 74 (2008) 5854-6.

[115] C. Varnado, D. Goodwin, System for the expression of recombinant hemoproteins in Escherichia coli, Protein Expression And Purification. (2004).

[116] C.L. Richard-Fogal, E.R. Frawley, R.E. Feissner, R.G. Kranz, Heme concentration dependence and metalloporphyrin inhibition of the system I and II cytochrome c assembly pathways., Journal Of Bacteriology. 189 (2007) 455-63.

[117] J. Woodward, N. Martin, M. Marletta, An Escherichia coli expression–based method for heme substitution, Nature Methods. (2006).

[118] I. Macdonald, A. Munro, W. Smith, Fatty Acid-Induced Alteration of the Porphyrin Macrocycle of Cytochrome P450 BM3, Biophysical Journal. (1998).

[119] L.C. Dickinson, J.C. Chien, Manganese cytochrome c. Structure and properties., The Journal Of Biological Chemistry. 252 (1977) 6156-62.

[120] K.M. Bennett, E.M. Shapiro, C.H. Sotak, A.P. Koretsky, Controlled aggregation of ferritin to modulate MRI relaxivity., Biophysical Journal. 95 (2008) 342-51.